Ab initio quantum direct dynamics simulations of ultrafast photochemistry with Multiconfigurational Ehrenfest approach

Dmitry V. Makhov [a], Christopher Symonds [a], Sebastian Fernandez-Alberti [b], Dmitrii V. Shalashilin [a,*]

[a] School of Chemistry, University of Leeds, Leeds LS2 9JT, United Kingdom
[b] Universidad Nacional de Quilmes/CONICET, Roque Saenz Peña 352, B1876BXD Bernal, Argentina

ARTICLE INFO

ABSTRACT

The Multiconfigurational Ehrenfest (MCE) method is a quantum dynamics technique which allows treatment of a large number of quantum nuclear degrees of freedom. This paper presents a review of MCE and its recent applications, providing a summary of the formalisms, including its *ab initio* direct dynamics versions and also giving a summary of recent results. Firstly, we describe the Multiconfigurational Ehrenfest version 2 (MCEv2) method and its applicability to direct dynamics and report new calculations which show that the approach converges to the exact result in model systems with tens of degrees of freedom. Secondly, we review previous "on the fly" *ab initio* Multiple Cloning (AIMC-MCE) MCE dynamics results obtained for systems of a similar size, in which the calculations treat every electron and every nucleus of a polyatomic molecule on a fully quantum basis. We also review the Time Dependent Diabatic Basis (TDDB) version of the technique and give an example of its application. We summarise the details of the sampling techniques and interpolations used for calculation of the matrix elements, which make our approach efficient. Future directions of work are outlined.

© 2017 The Authors. Published by Elsevier B.V. This is an open access article under the CC BY license (http://creativecommons.org/licenses/by/4.0/).

1. Introduction. Why AIMC-MCE?

In 1929 Dirac stated that: "The fundamental laws necessary for the mathematical treatment of a large part of physics and the whole of chemistry are thus completely known, and the difficulty lies only in the fact that application of these laws leads to equations that are too complex to be solved." Only recently however, eighty years later, have atomistic simulation methods started to emerge that allow the treatment of quantum systems with many degrees of freedom, overcoming the difficulty noted by Dirac. Several techniques now exist which can treat a large number of quantum degrees of freedom, albeit on a short time scale. Among them are methods of first principle Quantum Direct Dynamics (QDD). While these methods resemble first principle classical molecular dynamics, in which potential energies and forces are calculated by means of quantum mechanical electronic structure theories and codes, the quantum dynamics of nuclei in QDD is described not by a single trajectory but by an ensemble of trajectories weighted with their quantum amplitudes. This guided basis follows the most important parts of the wave packet and therefore minimises the number of necessary basis functions. Thus, in a certain sense, first principle QDD represents a "chemical quantum theory of everything" which relies solely on the most fundamental equations of quantum mechanics without approximations. Our existing *ab initio* Multiple Cloning Multiconfigurational Ehrenfest (AIMC-MCE) technique is an example of a first principle QDD approach based on the time dependent Schrödinger equation for both electrons and nuclei. We demonstrate that such an approach can work albeit on a short time scale.

Several methods exploiting the same general idea exist, which differ only by the type of guiding trajectories. To simulate the wave packet dynamics of nuclei, *Ab initio* Multiple Spawning (AIMS) [1] utilises ensembles of simple classical trajectories running on different electronic states. The method of Variational Multiconfigurational Gaussians (vMCG) relies on complicated non-classical variational trajectories [2–4]. The guiding trajectories of AIMC-MCE are in between AIMS and vMCG and combine some of their best features.

The Ehrenfest configuration is the central object of the AIMC-MCE approach, and serves as a time-dependent basis function. The Ehrenfest basis function $|\psi_n(t)\rangle$ is composed of nuclear and electronic parts:

$$|\psi_n(t)\rangle = |\chi_n(t)\rangle|\varphi_n(t)\rangle, \tag{1.1}$$

where the electronic part $|\varphi_n(t)\rangle$ is a superposition of several electronic eigenfunctions $|\phi_I\rangle$

* Corresponding author.
  E-mail address: d.shalashilin@leeds.ac.uk (D.V. Shalashilin).

$$|\varphi_n(t)\rangle = \sum_I a_I^{(n)}(t)|\phi_I\rangle, \tag{1.2}$$

and the nuclear part $|\chi_n(t)\rangle = |\chi_n(\overline{\mathbf{R}}_n(t), \overline{\mathbf{P}}_n(t))\rangle$ is a Gaussian Coherent State moving along an Ehrenfest trajectory $\overline{\mathbf{R}}_n(t), \overline{\mathbf{P}}_n(t)$. In coordinate representation

$$\chi_n(\mathbf{R}; \overline{\mathbf{R}}_n, \overline{\mathbf{P}}_n) = \langle \mathbf{R}|\chi_n(\overline{\mathbf{R}}_n, \overline{\mathbf{P}}_n)\rangle$$
$$= \left(\frac{2\alpha}{\pi}\right)^{N_{dof}/4} \exp\left(-\alpha(\mathbf{R}-\overline{\mathbf{R}}_n)^2 + \frac{i}{\hbar}\overline{\mathbf{P}}_n(\mathbf{R}-\overline{\mathbf{R}}_n) + \frac{i}{\hbar}\gamma_n(t)\right). \tag{1.3}$$

The parameter α here determines the width of the Gaussians, $\overline{\mathbf{R}}_n(t)$ and $\overline{\mathbf{P}}_n(t)$ are the phase space coordinate and momentum vectors of the n-th basis function centre, N_{dof} is the number of degrees of freedom, and γ_n is a phase. The width parameter α can be taken, for example, according to previous prescriptions [5], which are based on the optimization for a reference set of over 100 molecules.

A single Ehrenfest configuration is not flexible enough to accurately describe full quantum dynamics. In the MCE approach, multiple Ehrenfest configurations are used and these represent a basis set in which the total wave-function is expanded such that:

$$|\Psi(t)\rangle = \sum_n c_n(t)|\psi_n(t)\rangle. \tag{1.4}$$

The evolution of the Ehrenfest amplitudes $a_I^{(n)}$, the momenta $\overline{\mathbf{P}}_n$ and positions $\overline{\mathbf{R}}_n$ of the wave packets are driven by the Ehrenfest equations, while the equations for the amplitudes $c_n(t)$, which follow from the Schrödinger equation, describe coherent coupling between Ehrenfest configurations making the approach formally exact [6–10]. The AIMC-MCE approach has a number of features distinguishing it from the competing techniques

1) The Ehrenfest trajectories are nonclassical in a similar fashion to those of vMCG. In regions of strong non-adiabatic coupling the basis follows the dynamics of the quantum wave packet more accurately than the simple classical trajectories employed by AIMS. It is well known however that the Ehrenfest equations of motion can be problematic after passing a strong coupling region, where the Ehrenfest trajectories guided by a potential energy surface average of those of individual electronic states may move outside of the dynamically important region. This is remedied in the AIMC-MCE method by a procedure called cloning [6,7], which is an adaptation of the spawning procedure of AIMS [1]. After cloning, an Ehrenfest configuration (1.1) yields two configurations such that the first "clone" has nonzero amplitude for only one electronic state, and the second contains contributions of all other electronic states. Thus, cloning reprojects the Ehrenfest trajectories on the individual electronic states after quantum transitions are completed. Importantly, this projection is done in a manner that does not alter the nuclear wave-function at the time of cloning (similar to spawning in AIMS). The cloned basis functions form an efficient adoptive basis which follow the quantum wave packet dynamics very efficiently. Thus the AIMC-MCE method combines the best feature of AIMS and vMCG methods.

2) AIMC-MCE uses an interpolation procedure for calculating matrix elements that is based *solely* on quantities calculated at the centres of the time dependent Gaussians (1.3). There are no calculations of energies, gradients, or non-adiabatic coupling matrix elements at intermediate geometries between trajectory centres; this minimizes the number of computationally expensive calls of the *ab initio* electronic structure code. Moreover, a large number of underlying Ehrenfest trajectories can be run independently and then later recombined in a "post-processing" procedure, which calculates the quantum amplitudes $c_n(t)$ in (1.4) with quantum mechanical coupling between the time-dependent Ehrenfest basis functions (1.1) computed from the trajectory data at low computational cost. This feature is not possible in the vMCG method.

3) AIMC-MCE uses an incremental propagation procedure, which we refer to as "bit-by-bit" propagation, in which the propagation of a large basis is replaced by a large number of Monte-Carlo repetitions of the wave-function "bits", each of them using a smaller basis. The incremental propagation procedure is not an approximation, as it exploits the linearity of the Schrödinger equations to make basis set sampling more efficient [11].

4) AIMC-MCE makes use of the idea of train basis sets [6,12,13], also known as time displaced basis sets. Basis functions in the train follow each other along the same Ehrenfest trajectory but with a time delay, so that propagating the trains does not require any additional electronic structure calculations. The trains serve to increase the original basis set by orders of magnitude, reducing the noise and improving the quality of quantum dynamics calculations at almost no extra cost.

As a result of all above features AIMC-MCE allows statistics unmatched by other quantum *ab initio* direct dynamics methods. It can afford basis sets comprised of thousands of coupled configurations. With the use of hundreds and even thousands of wave-function "bits", the total number of TBFs used can reach hundreds of thousands. Due to the high cost of electronic structure calculations, total CPU time can reach hundreds of years, but incremental propagation of "bits" and the postprocessing procedure for quantum coupling allows running Ehrenfest trajectories one-by-one independently from each other, which can be easily parallelized. It will be shown below that MCE can converge to the exact quantum results when applied to model systems.

2. Theory – Working equations

MCE is an efficient tool for both on-the-fly *ab initio* non-adiabatic dynamics of real molecules and for the simulation of model systems, such as the spin boson model [14]. Although MCE treats, in principle, all degrees of freedom (DOFs) on a fully quantum level, some of these DOFs are "more quantum" than others. For example electronic degrees of freedom are always "more quantum" than those of nuclear motion. Thus, while the electronic part of the wave-function is represented in an accurate regular basis $|\phi_I\rangle$, the wave-function for nuclear coordinates $\mathbf{R}$ is represented in a trajectory-guided Gaussian basis $|\chi_n(\overline{\mathbf{R}}_n, \overline{\mathbf{P}}_n)\rangle$. The choice of the electronic basis depends on many factors. It is often convenient to use a diabatic basis for model systems, as in this case it frequently allows a better representation with the smoothest changes of coefficients. Real molecular systems simulated using on-the-fly *ab initio* calculations however require an adiabatic or time-dependent diabatic (TDD) basis.

Below we use the following notations: 1) diabatic electronic states that do not depend on nuclear coordinates $\mathbf{R}$ are referred as $|\phi_I\rangle$, 2) adiabatic states are referred as $|\phi_I(\mathbf{R})\rangle$, and 3) TDD states that are the same adiabatic states taken in the centre of nth Gaussian $\overline{\mathbf{R}}_n$ are referred to either as $\left|\phi_I(\overline{\mathbf{R}}_n(t))\right\rangle$ or just $\left|\phi_I^{(n)}\right\rangle$ in order to shorten long equations (i.e. $\left|\phi_I^{(n)}\right\rangle \equiv \left|\phi_I(\overline{\mathbf{R}}_n(t))\right\rangle$. We mostly omit obvious arguments, such as electronic coordinates $\mathbf{r}$ in $|\phi_I\rangle$, $|\phi_I(\mathbf{R})\rangle$, and $\left|\phi_I^{(n)}\right\rangle$ and write all integrals in bra-ket notation, e.g. we write $\langle\chi_m\phi_I|\widehat{V}|\phi_J\chi_n\rangle$ instead of $\int d\mathbf{R}\chi_m(\mathbf{R}; \overline{\mathbf{R}}_m, \overline{\mathbf{P}}_m)^* \chi_n(\mathbf{R}; \overline{\mathbf{R}}_n, \overline{\mathbf{P}}_n) \int d\mathbf{r}\phi_I(r)^* V(\mathbf{r}, \mathbf{R})\phi_J(\mathbf{r})$.

2.1. MCE in a diabatic basis

The propagation of a total wave-function in a trajectory-guided basis is determined by the time-dependence of the positions and momenta of all Gaussians and the time-dependence of the corresponding quantum amplitudes in (1.2), (1.4) or (2.1.6). The best possible time-evolution for a given set of parameters determining a wave-function can be found from the variational principle [15], as is done in vMCG [2–4] and in similar G-MCTDH methods [16]. The problem is that these equations are very complicated and unstable. They also cannot be parallelized easily, as all positions, momenta and quantum amplitudes are coupled together. So, the MCE method uses instead a simpler procedure, where each trajectory is guided by its own Ehrenfest force:

$$\mathbf{F}_n = \frac{-\frac{d}{d\mathbf{R}_n}\langle\psi_n|\hat{H}|\psi_n\rangle}{\langle\psi_n|\psi_n\rangle}. \tag{2.1.1}$$

The Hamiltonian is a sum of the nuclear kinetic energy operator $\hat{T} = -\frac{\hbar^2}{2\mathbf{M}}\frac{d^2}{d\mathbf{R}^2}$ (where the notation $\frac{1}{\mathbf{M}}$ refers to a diagonal matrix of the inverse masses of the atoms) and the potential energy operator $\hat{V}$:

$$\hat{H} = \hat{T} + \hat{V}. \tag{2.1.2}$$

As the electronic diabatic basis functions $|\phi_I\rangle$ here do not depend on $\mathbf{R}$, we can write:

$$\langle\psi_n|\hat{H}|\psi_n\rangle = \langle\chi_n|\hat{T}|\chi_n\rangle + \sum_{I,J}a_I^{(n)*}a_J^{(n)}\langle\chi_n\phi_I|\hat{V}|\phi_J\chi_n\rangle. \tag{2.1.3}$$

The kinetic energy matrix element

$$\langle\chi_n|\hat{T}|\chi_n\rangle = \frac{(\overline{\mathbf{P}}_n^2 + \alpha\hbar^2)}{2\mathbf{M}} \tag{2.1.4}$$

does not depend on $\overline{\mathbf{R}}_n$, so for the Ehrenfest force we obtain:

$$\mathbf{F}_n = \frac{-\sum_{I,J}a_I^{(n)*}a_J^{(n)}\frac{d}{d\overline{\mathbf{R}}_n}\langle\chi_n\phi_I|\hat{V}|\phi_J\chi_n\rangle}{\sum_I a_I^{(n)*}a_I^{(n)}}. \tag{2.1.5}$$

In our previous works two different versions of MCE, referred as MCEv1 and MCEv2, were introduced [11,14] using two possible forms for the ansatz of the wave-function. The exact meaning and time evolution of the Ehrenfest amplitudes $a_I^{(n)}(t)$ are different for MCEv1 and MCEv2. In the MCEv1 formulation, each amplitude $a_I^{(n)}(t)$ determines a contribution of an Ith state of the nth configuration into a wave-function:

$$|\Psi(t)\rangle = \sum_n |\chi_n\rangle\left(\sum_I a_I^{(n)}(t)|\phi_I\rangle\right), \tag{2.1.6}$$

and the time evolution of these amplitudes is obtained through the variational principle as

$$\sum_n\langle\chi_m|\chi_n\rangle\dot{a}_I^{(n)} = -\frac{i}{\hbar}\sum_n\left(\sum_J\left(\langle\chi_m\phi_I|\hat{H}|\chi_n\phi_J\rangle a_J^{(n)}\right) - i\left\langle\chi_m\left|\frac{\partial\chi_n}{\partial t}\right.\right\rangle a_I^{(n)}\right), \tag{2.1.7}$$

where

$$\left\langle\chi_m\left|\frac{d\chi_n}{dt}\right.\right\rangle = \left(\dot{\overline{\mathbf{R}}}_n\left\langle\chi_m\left|\frac{d}{d\overline{\mathbf{R}}_n}\right|\chi_n\right\rangle + \dot{\overline{\mathbf{P}}}_n\left\langle\chi_m\left|\frac{d}{d\overline{\mathbf{P}}_n}\right|\chi_n\right\rangle\right) + \frac{i}{\hbar}\dot{\gamma}_n\langle\chi_n|\chi_m\rangle. \tag{2.1.8}$$

It can be seen from Eq. (2.1.7) that all amplitudes $a_I^{(n)}$ of all electronic states (I) and all trajectories (n) are coupled with each other. This means that the Ehrenfest trajectories given by (2.1.5) are not

independent: they influence each other via the Eq. (2.1.8), and the motion of all trajectory basis functions (TBFs) in the MCEv1 approach is coupled through the Ehrenfest amplitudes. The MCEv1 formulation was shown to be able to successfully simulate systems of up to 2000 degrees of freedom [14], which implies that MCEv1 is a very efficient method for treating multidimensional systems. However the coupling between trajectories makes MCEv1 hard to implement in *ab initio* direct dynamics context.

To remedy the above difficulties, the MCEv2 [11] approach was formulated. MCEv2 uses a different form for the ansatz,

$$|\Psi(t)\rangle = \sum_n c_n(t)|\chi_n\rangle\left(\sum_I a_I^{(n)}(t)|\phi_I\rangle\right), \tag{2.1.9}$$

where a separate set of amplitudes $c_n(t)$ is used to describe the contributions of each configuration into a wave-function, while the amplitudes $a_I^{(n)}(t)$ now determine only the contribution of each quantum state into the nth Ehrenfest configuration. As a result, the coupling between the trajectories and the coupling between the electronic states are now separated. The amplitudes $a_I^{(n)}(t)$ in the MCEv2 approach are normalized for each TBF

$$\sum_I a_I^{(n)*}a_I^{(n)} = 1, \tag{2.1.10}$$

and Eq. (2.1.5) for the Ehrenfest force takes the form:

$$\mathbf{F}_n = -\sum_{I,J}a_I^{(n)*}a_J^{(n)}\frac{d}{d\overline{\mathbf{R}}_n}\langle\chi_n\phi_I|\hat{V}|\phi_J\chi_n\rangle. \tag{2.1.11}$$

The time evolution of amplitudes $a_I^{(n)}(t)$ for each trajectory in the MCEv2 approach depends only on the motion of this particular TBF:

$$\dot{a}_I^{(n)} = -\frac{i}{\hbar}\sum_J\langle\chi_n\phi_I|\hat{H}|\chi_n\phi_J\rangle a_J^{(n)} - \left\langle\chi_n\left|\frac{\partial\chi_n}{\partial t}\right.\right\rangle a_I^{(n)}. \tag{2.1.12}$$

Let us introduce, as is normally done, the evolution of the phase γ_n as:

$$\frac{d\gamma_n}{dt} = \frac{\overline{\mathbf{P}}_n\dot{\overline{\mathbf{R}}}_n}{2}. \tag{2.1.13}$$

Then, substituting this into (2.1.8) and using the following expressions for the matrix elements of the Gaussians

$$\left\langle\chi_n\left|\frac{d}{d\overline{\mathbf{R}}_n}\right|\chi_n\right\rangle = -\frac{i}{\hbar}\overline{\mathbf{P}}_n, \tag{2.1.14}$$

$$\left\langle\chi_n\left|\frac{d}{d\overline{\mathbf{P}}_n}\right|\chi_n\right\rangle = 0, \tag{2.1.15}$$

we obtain

$$\left\langle\chi_n\left|\frac{\partial\chi_n}{\partial t}\right.\right\rangle = -\frac{i}{2\hbar}\dot{\overline{\mathbf{R}}}_n\overline{\mathbf{P}}_n. \tag{2.1.16}$$

Now, substituting (2.1.3), (2.1.4) and (2.1.16) into (2.1.12) and ignoring a small second term in (2.1.4) associated with Gaussian width, we obtain a final equation for the evolution of Ehrenfest amplitudes in the MCEv2 approach:

$$\dot{a}_I^{(n)} = -\frac{i}{\hbar}\sum_J\langle\chi_n\phi_I|\hat{V}|\chi_n\phi_J\rangle a_J^{(n)}. \tag{2.1.17}$$

Thus in the MCEv2 approach, there is no coupling between coefficients $a_I^{(n)}$ for different Ehrenfest configurations (n). Instead, the quantum coupling between trajectories in MCEv2 is described by the time-evolution of amplitudes $c_n(t)$, which can be found by substituting the wave-function ansatz (1.4) into the time-dependent Schrödinger equation:

$$\sum_n \langle \psi_m | \psi_n \rangle \dot{c}_n = -\frac{i}{\hbar} \sum_n \left(\langle \psi_m | \hat{H} | \psi_n \rangle - i \langle \psi_m | \frac{\partial \psi_n}{\partial t} \rangle \right) c_n, \qquad (2.1.18)$$

where

$$\langle \psi_m | \psi_n \rangle = \langle \chi_m | \chi_n \rangle \sum_I \left(a_I^{(m)} \right)^* a_I^{(n)}, \qquad (2.1.19)$$

$$\langle \psi_m | \hat{H} | \psi_n \rangle = \sum_{I,J} \langle \chi_m \phi_I | \hat{H} | \chi_n \phi_J \rangle \left(a_I^{(m)} \right)^* a_J^{(n)}, \qquad (2.1.20)$$

and

$$\langle \psi_m | \frac{\partial \psi_n}{\partial t} \rangle = \langle \chi_m | \frac{\partial \chi_n}{\partial t} \rangle \sum_I \left(a_I^{(m)} \right)^* a_I^{(n)} + \langle \chi_m | \chi_n \rangle \sum_I \left(a_I^{(m)} \right)^* \frac{\partial}{\partial t} a_I^{(n)}. \qquad (2.1.21)$$

The absence of coupling between amplitudes $a_I^{(n)}$ for different trajectories means that the TBFs in the MCEv2 formulation move independently from each other, which significantly simplifies the computational procedure and makes MCEv2 a method of choice for the direct *ab initio* dynamics. Eqs. (2.1.11) and (2.1.17)–(2.1.21) form a complete set for calculating time evolution of the wave-function in the MCEv2 approach. These equations, while different in notation, are identical to those of Ref. [11].

2.2. Ab initio MCE in an adiabatic basis

Although a diabatic basis is often convenient for model calculations, it is inappropriate for *ab initio* non-adiabatic direct dynamics of the molecules. The electronic structure calculations are usually performed only for several lowest electronic states, and these wave-functions strongly depend on nuclear coordinates. In order to address this, we can reformulate the MCEv2 approach in an adiabatic basis $|\phi_I(\mathbf{R})\rangle$. The electronic coordinates $\mathbf{r}$ are omitted to make the equations shorter.

Unlike the case of diabatic representation, the potential energy operator $\hat{V}$ is diagonal in the adiabatic basis

$$\langle \phi_I(\mathbf{R}) | \hat{V}(\mathbf{R}) | \phi_J(\mathbf{R}) \rangle = V_I(\mathbf{R}) \delta_{IJ}, \qquad (2.2.1)$$

and the coupling between electronic states originates from off-diagonal matrix elements of the kinetic energy operator, which are non-zero because of the parametric dependence of the electronic wave-functions on the coordinates $\mathbf{R}$ of the nuclei.

Computing the matrix elements of $\hat{V}$ requires the potential energy surfaces $V_I(\mathbf{R})$ generated by electronic structure calculations, which are the most expensive part of *ab initio* dynamics. Therefore, we must apply approximations in order to minimize the cost and to obtain these matrix elements using a small number of electronic structure calculations for few nuclear geometries. In *ab initio* MCE approach, the diagonal matrix elements are approximated by the potential energies in the centres instead of averaging over Gaussians:

$$\langle \chi_n | V_I(\mathbf{R}) | \chi_n \rangle \approx V_I(\bar{\mathbf{R}}_n). \qquad (2.2.2)$$

For matrix elements between different trajectories, the first-order bra-ket averaged Taylor (BAT) expansion [6] is applied:

$$\langle \chi_m | V_I(\mathbf{R}) | \chi_n \rangle \approx \frac{1}{2} \langle \chi_m | \chi_n \rangle (V_I(\bar{\mathbf{R}}_m) + V_I(\bar{\mathbf{R}}_n))$$
$$+ \frac{1}{2} \langle \chi_m | (\mathbf{R} - \bar{\mathbf{R}}_m) | \chi_n \rangle \frac{d}{d\bar{\mathbf{R}}_m} V_I(\bar{\mathbf{R}}_m)$$
$$+ \frac{1}{2} \langle \chi_m | (\mathbf{R} - \bar{\mathbf{R}}_n) | \chi_n \rangle \frac{d}{d\bar{\mathbf{R}}_n} V_I(\bar{\mathbf{R}}_n). \qquad (2.2.3)$$

Approximation (2.2.3) uses energies and gradients only from the centres of the Gaussians, which are calculated anyway to find the Ehrenfest trajectories guiding the basis. The matrix elements given by this approximation are used to solve quantum coupling equations (2.1.18) that give amplitudes $c_n(t)$ in the wave-function representation (2.1.9). Thus, unlike the saddle point approximation (SPA) [1], approximation (2.2.3) provides the interaction between trajectories at practically no additional computational cost. Note that the first-order term is extremely important here, as the one-way transfer of quantum amplitude between different Gaussians is driven by the imaginary part of the prefactor of the matrix elements of the Hamiltonian. If two Gaussians differ mostly by the coordinates, the transfer of amplitude reflects the motion of the atoms; in this case it is driven by the imaginary part of the prefactor for the kinetic energy matrix elements, which is proportional to the average momentum and is always taken into account (see Eq. (2.2.7) below). In the case where two Gaussians differ mostly by the momenta, the transfer of quantum amplitude reflects the acceleration, and is guided by the imaginary part of the prefactor for the potential energy matrix elements, which is proportional to the gradients and is given in our approximation by the first order term in (2.2.3).

Because of the dependence of adiabatic electronic wave-functions on nuclear coordinates $\mathbf{R}$, the kinetic energy operator $\hat{T}$ provides the non-adiabatic interstate coupling. Disregarding, as is normally done, the second derivatives $d^2 | \phi_I(\mathbf{R}) \rangle / d\mathbf{R}^2$ which, by experience [17], have a negligible effect on the nuclear dynamics and using an approximation similar to (2.2.2), we get:

$$\langle \chi_n \phi_I(\mathbf{R}) | \hat{T} | \phi_J(\mathbf{R}) \chi_n \rangle \approx -\frac{\hbar^2}{2\mathbf{M}} \langle \chi_n \phi_I(\mathbf{R}) | \phi_J(\mathbf{R}) \frac{d^2 \chi_n}{d\mathbf{R}^2} \rangle$$
$$-\frac{\hbar^2}{\mathbf{M}} \langle \chi_n \phi_I(\mathbf{R}) | \frac{d\phi_J(\mathbf{R})}{d\mathbf{R}} \frac{d\chi_n}{d\mathbf{R}} \rangle \approx \frac{\bar{\mathbf{P}}_n^2}{2\mathbf{M}} \delta_{IJ} - i\hbar \frac{\bar{\mathbf{P}}_n^2}{\mathbf{M}} \mathbf{d}_{IJ}^{(n)}, \qquad (2.2.4)$$

where

$$\mathbf{d}_{IJ}^{(n)} = \langle \phi_I(\mathbf{R}) | \frac{d\phi_J(\mathbf{R})}{d\mathbf{R}} \rangle \Big|_{\mathbf{R}=\bar{\mathbf{R}}_n} \qquad (2.2.5)$$

are the non-adiabatic coupling matrix elements (NACMEs). For the matrix elements of $\hat{T}$ between the trajectories, a simple approximation is used:

$$\langle \chi_m \phi_I | \hat{T} | \phi_J \chi_n \rangle \approx \langle \chi_m | \hat{T} | \chi_n \rangle \delta_{IJ} - i\hbar \frac{\bar{\mathbf{P}}_n}{2\mathbf{M}} \left(\mathbf{d}_{IJ}^{(m)} + \mathbf{d}_{IJ}^{(n)} \right), \qquad (2.2.6)$$

where

$$\langle \chi_m | \hat{T} | \chi_n \rangle = \frac{1}{2\mathbf{M}} \left[((\bar{\mathbf{P}}_n + \bar{\mathbf{P}}_m)/2)^2 + \alpha \hbar^2 - \alpha^2 (\bar{\mathbf{R}}_n - \bar{\mathbf{R}}_m)^2 \hbar^2 \right.$$
$$\left. - i\alpha(\bar{\mathbf{R}}_n - \bar{\mathbf{R}}_m)(\bar{\mathbf{P}}_n + \bar{\mathbf{P}}_m)\hbar \right] \langle \chi_m | \chi_n \rangle. \qquad (2.2.7)$$

The expression for the force driving Ehrenfest trajectories in an adiabatic basis

$$\mathbf{F}_n = -\sum_I a_I^{(n)*} a_I^{(n)} \frac{d}{d\bar{\mathbf{R}}_n} V_I + \sum_{I \neq J} a_I^{(n)*} a_J^{(n)} \mathbf{d}_{IJ}^{(n)} (V_I - V_J) \qquad (2.2.8)$$

is different from the expression for the force in a diabatic basis (2.1.11). One can see that together with a usual gradient term, Eq. (2.2.8) also includes a second term that compensates for the potential energy change associated with non-adiabatic electronic population transfer. This force is often called the Hellmann-Feynman force. The values of NACMEs entering this second term are calculated by electronic structure codes alongside with potential energies and their gradients. A detailed derivation of Eq. (2.2.8) is given in the Appendix A.

The motion of each TBF (1.1) is coupled with the evolution of the Ehrenfest amplitudes $a_I^{(n)}$, which is also different here from the one in a diabatic basis given by (2.1.17). Substituting (2.2.1), (2.1.16) and approximations (2.2.2), (2.2.4) into Eq. (2.1.12), we obtain

$$\dot{a}_I^{(n)} = -\frac{i}{\hbar}\sum_J H_{IJ}^{eff\,(n)} a_J^{(n)},\tag{2.2.9}$$

where the matrix elements of the effective Hamiltonian $H_{IJ}^{eff\,(n)}$ are expressed as:

$$H_{IJ}^{eff\,(n)} = \begin{cases} V_I(\overline{\mathbf{R}}_n), & I=J \\ -i\hbar\,\overline{\mathbf{P}}_n\mathbf{M}^{-1}\mathbf{d}_{IJ}^{(n)}, & I\neq J \end{cases}.\tag{2.2.10}$$

In the above, we used time evolution of the nuclear phase γ_n given by Eq. (2.1.13), the same as in a diabatic basis, which cancels the diagonal matrix elements of the kinetic energy operator. Eqs. (2.2.8)–(2.2.10) form a complete set of equations determining the evolution of the Ehrenfest TBFs $|\psi_n(t)\rangle$. The evolution of the amplitudes $c_n(t)$ is described, as before, by Eq. (2.1.18), where approximations (2.2.3) and (2.2.6) are used to calculate the matrix elements between different trajectories.

2.3. Ab initio MCE in a time-dependent diabatic basis (TDDB)

The MCE approach in an adiabatic electronic basis has been used by us to simulate the photodynamics of ethylene after $\pi \rightarrow \pi^*$ excitation [6] and the photodissociation of pyrrole [7], where it worked well. However, this version of the method can fail for large conjugated molecules where electronic states can change significantly on the length-scale of the Gaussian width. In particular, the wave-function can change instantly at trivial unavoided crossings [18] where two electronic states localized on two spatially separated parts of a large molecule change their order. To remedy this, another version of the method, Multiconfigurational Ehrenfest in time-dependent diabatic basis (MCE-TDDB), was developed [19]. In this version of MCE, each Gaussian trajectory carries its own time-dependent diabatic electronic basis that coincides with adiabatic basis in the centre of the Gaussian:

$$\left|\phi_I^{(n)}\right\rangle = \left|\phi_I(\overline{\mathbf{R}}_n(t))\right\rangle.\tag{2.3.1}$$

The new electronic basis functions $\left|\phi_I^{(n)}\right\rangle$ do not depend explicitly on $\mathbf{R}$ as is customary in many theories of non-adiabatic coupling. Instead the coupling now originates from the time-dependence of the electronic basis functions through the motion of $\overline{\mathbf{R}}_n$. We would like to emphasize that the "time-dependent diabatic basis" used here should not be confused with the "diabatic basis" used in Section 2.1; the trajectories here are still calculated using Eqs. (2.2.8)–(2.2.10) for an adiabatic basis (see below), and the new representation affects only matrix elements between different TBFs.

It was shown in Ref. [6] that the TDDB representation leads to the same set of final equations as the adiabatic one when the electronic wave-function does not depend too strongly on the nuclear coordinates. However, in this section we are considering a different case when the overlaps between the electronic eigenstates belonging to the different Gaussians $\left\langle\phi_I^{(n)}\middle|\phi_J^{(m)}\right\rangle$ can be very far from Kronecker's δ_{IJ}, even when these Gaussians are sufficiently close to each other and nuclear parts have a significant overlap. In this situation, these overlaps must be taken into account accurately. In principle, they can be calculated directly, but it is more convenient to propagate them together with the basis. The following equation for the time-dependence of the overlap integrals is used:

$$\frac{d}{dt}\left\langle\phi_I^{(m)}\middle|\phi_J^{(n)}\right\rangle = \dot{\overline{\mathbf{R}}}_m\sum_K\left\langle\phi_K^{(m)}\middle|\phi_J^{(n)}\right\rangle\mathbf{d}_{KI}(\overline{\mathbf{R}}_m)$$
$$+\dot{\overline{\mathbf{R}}}_n\sum_K\left\langle\phi_I^{(m)}\middle|\phi_K^{(n)}\right\rangle\mathbf{d}_{KJ}(\overline{\mathbf{R}}_n).\tag{2.3.2}$$

Because summation in Eq. (2.3.2) is limited to only a few lowest electronic states for which NACMEs are calculated, in practice this method may slightly overestimate the electronic overlaps. Nevertheless, the accuracy of this approximation is compatible with the accuracy of other approximations used in this approach. The overlap matrices $\left\langle\phi_I^{(n)}\middle|\phi_J^{(m)}\right\rangle$ trace the difference between adiabatic electronic states for each pair of trajectories. Along with the difference in the order of states, it would also reflect the difference of their signs, known as the geometric phase effect [20,21], which can appear when a pair of trajectories passes on two different sides of a conical intersection. Thus, unlike adiabatic representation, a TDD basis naturally accounts for the geometric phase. Although it is unclear whether geometric phase can significantly affect direct dynamics simulations of multidimensional systems, for small low dimensionality systems it is certainly important.

It is easy to show (see Appendix A) that the evolution of TBFs in the MCE-TDBB method is described by the same set of equations as in the adiabatic basis. The difference between the MCE and MCE-TDDB approaches is in the time evolution of amplitudes $c_n(t)$: although it is determined by the same Eq. (2.1.18), the matrix elements between trajectories are different. The overlaps now include both the nuclear and electronic parts,

$$\langle\psi_m(t)|\psi_n(t)\rangle = \langle\chi_m|\chi_n\rangle\sum_{I,J}\left(a_I^{(m)}\right)^* a_J^{(n)}\left\langle\phi_I^{(m)}\middle|\phi_J^{(n)}\right\rangle,\tag{2.3.3}$$

as the overlap between electronic functions is not a simple Kronecker's delta $\left\langle\phi_I^{(m)}\middle|\phi_J^{(n)}\right\rangle\neq\delta_{IJ}$.

Similarly, for kinetic energy matrix elements, we have:

$$\left\langle\chi_m\phi_I^{(m)}\middle|\hat{T}\middle|\chi_n\phi_J^{(n)}\right\rangle = \left\langle\chi_m\middle|-\frac{\hbar^2}{2\mathbf{M}}\frac{d^2}{d\mathbf{R}^2}\middle|\chi_n\right\rangle\left\langle\phi_I^{(m)}\middle|\phi_J^{(n)}\right\rangle.\tag{2.3.4}$$

For the potential energy matrix, we use an approximation similar to the first order BAT expansion applied above in the case of the adiabatic representation:

$$\left\langle\chi_m\phi_I^{(m)}\middle|\hat{V}(\mathbf{R})\middle|\chi_n\phi_J^{(n)}\right\rangle \approx \frac{1}{2}\left\langle\phi_I^{(m)}\middle|\phi_J^{(n)}\right\rangle\Big\{\langle\chi_m|\chi_n\rangle\left[V_I(\overline{\mathbf{R}}_m)+V_J(\overline{\mathbf{R}}_n)\right]$$
$$+\left\langle\chi_m\middle|\left[(\mathbf{R}-\overline{\mathbf{R}}_m)\cdot\frac{d}{d\overline{\mathbf{R}}_m}V_I(\overline{\mathbf{R}}_m)\right]+\left[(\mathbf{R}-\overline{\mathbf{R}}_n)\cdot\frac{d}{d\overline{\mathbf{R}}_n}V_J(\overline{\mathbf{R}}_n)\right]\middle|\chi_n\right\rangle\Big\}\tag{2.3.5}$$

which again differs from (2.2.3) by the presence of the overlap $\left\langle\phi_I^{(m)}\middle|\phi_J^{(n)}\right\rangle$ of electronic wave-functions belonging to different Ehrenfest configurations or TBFs. Finally, the term $\langle\psi_m(t)|\frac{d}{dt}|\psi_n(t)\rangle$ in Eq. (2.1.18) is now written as:

$$\left\langle\psi_m\middle|\frac{d\psi_n}{dt}\right\rangle = \left\langle\chi_m\middle|\frac{d\chi_n}{dt}\right\rangle\sum_{I,J}\left\langle\phi_I^{(m)}\middle|\phi_J^{(n)}\right\rangle\left(a_I^{(m)}\right)^* a_J^{(n)} - \frac{i}{\hbar}$$
$$\times\langle\chi_m|\chi_n\rangle\sum_{I,J}\left\langle\phi_I^{(m)}\middle|\phi_J^{(n)}\right\rangle\left(a_I^{(m)}\right)^* a_J^{(n)}V_J(\overline{\mathbf{R}}_n).\tag{2.3.6}$$

More details on the approximations used for matrix elements between different trajectories in the TDD representation are given in the Appendix A.

The interpretation of the results of MCE-TDDB calculations, for example population analysis, is non-trivial because the nature of electronic states can change very quickly and their order can be

different for different basis functions. A special procedure must be applied for calculating electronic properties.

For population analysis, let us introduce the adiabatic population operator

$$\hat{P}_K(\mathbf{R}) = |\phi_K(\mathbf{R})\rangle\langle\phi_K(\mathbf{R})|, \quad (2.3.7)$$

where, as before, $|\phi_K(\mathbf{R})\rangle$ are the adiabatic electronic eigenfunctions. Then, the electronic state populations can be expressed as:

$$P_K = \left\langle \Psi \middle| \hat{P}_K \middle| \Psi \right\rangle$$
$$= \sum_{m,n} c_m^* c_n \sum_{I,J} \left(a_I^{(m)}\right)^* a_J^{(n)} \left\langle \chi_m \middle| \left\langle \phi_I^{(m)} \middle| \phi_K(\mathbf{R}) \right\rangle \left\langle \phi_K(\mathbf{R}) \middle| \phi_J^{(n)} \right\rangle \middle| \chi_n \right\rangle. \quad (2.3.8)$$

Using an approximation similar to the one used for other matrix elements between trajectories (see Appendix A), we can write

$$P_K = \frac{1}{2}\sum_{m,n} c_m^* c_n \langle\chi_m|\chi_n\rangle \sum_{I,J}\left(a_I^{(m)}\right)^* a_J^{(n)}\left\{\left\langle\phi_K^{(m)}\middle|\phi_J^{(n)}\right\rangle\delta_{IK}\right.$$
$$\left. +\left\langle\phi_I^{(m)}\middle|\phi_K^{(n)}\right\rangle\delta_{JK}\right\}, \quad (2.3.9)$$

which can be simplified to

$$P_K = \mathrm{Re}\left\{\sum_{m,n} c_m^* c_n \langle\chi_m|\chi_n\rangle\left(a_K^{(m)}\right)^*\sum_I a_I^{(n)}\left\langle\phi_K^{(m)}\middle|\phi_I^{(n)}\right\rangle\right\}. \quad (2.3.10)$$

The same approach can be applied for the calculation of any other electronic property. If this property can be described by a quantum operator $\hat{N}$, then

$$\left\langle\hat{N}\right\rangle = \sum_{m,n} c_m^* c_n \sum_{I,J}\left(a_I^{(m)}\right)^* a_J^{(n)}\left\langle\chi_m\middle|\left\langle\phi_I^{(m)}\middle|\hat{N}\middle|\phi_J^{(n)}\right\rangle\middle|\chi_n\right\rangle. \quad (2.3.11)$$

Using the same approximation as in (2.3.9) and assuming that $\hat{N}$ is real and depends only on the electronic degrees of freedom, we get:

$$\left\langle\hat{N}\right\rangle = \mathrm{Re}\left\{\sum_{m,n} c_m^* c_n \langle\chi_m|\chi_n\rangle\sum_{I,J,K}\left(a_I^{(m)}\right)^* a_J^{(n)}\left\langle\phi_K^{(m)}\middle|\phi_J^{(n)}\right\rangle N_{IK}^{(m)}\right\}, \quad (2.3.12)$$

where $N_{IK}^{(m)} = \left\langle\phi_I^{(m)}\middle|\hat{N}\middle|\phi_K^{(m)}\right\rangle$ are the matrix elements of the operator $\hat{N}$ between eigenstates for the centre of the mth Gaussian, which can be easily calculated from the electronic structure data for the trajectories.

3. Basis set sampling techniques for *ab initio* MCE dynamics

Sampling a basis of Gaussians such that it would represent well the molecule wave-function for a long time is key to the efficiency of trajectory based methods. However, there are several problems which make sampling difficult. Firstly, full sampling of the initial wave packet in systems with many degrees of freedom is practically impossible. Secondly, in multidimensional systems the Gaussians run away from each other, their overlaps tend to zero, and the coupling between them is lost very quickly. Thirdly, after a while the Ehrenfest trajectories start to misguide the basis and it no longer follows the wave-function in phase space. In this section we will describe the algorithms which have been developed to address these issues.

3.1. Bit-by-bit propagation

Bit-by-bit propagation addresses the first problem mentioned above. Often, a multidimensional wave-function is complicated

and cannot be easily represented on a small basis of coherent states. One can however decompose it into a superposition of a number of coherent states by inserting the coherent state identity operator $\hat{I} = \int |\chi(\overline{\mathbf{R}}_0, \overline{\mathbf{P}}_0)\rangle\frac{d^2\overline{\mathbf{R}}_0, \overline{\mathbf{P}}_0}{(2\pi\hbar)^M}\langle\chi(\overline{\mathbf{R}}_0, \overline{\mathbf{P}}_0)|$ as follows

$$|\Psi(0)\rangle = \int |\chi(\overline{\mathbf{R}}_0, \overline{\mathbf{P}}_0)\rangle\frac{d^2\overline{\mathbf{R}}_0, \overline{\mathbf{P}}_0}{(2\pi\hbar)^M}\langle\chi(\overline{\mathbf{R}}_0, \overline{\mathbf{P}}_0)|\Psi(0)\rangle. \quad (3.1.1)$$

Following this, one can propagate each Gaussian $|\chi(\overline{\mathbf{R}}_0, \overline{\mathbf{P}}_0)\rangle$ in the expansion (3.1.1) individually and represent the total time dependent wave-function as a superposition

$$e^{-\frac{i}{\hbar}\hat{H}t}|\Psi(0)\rangle = \int e^{-\frac{i}{\hbar}\hat{H}t}|\chi(\overline{\mathbf{R}}_0, \overline{\mathbf{P}}_0)\rangle\frac{d^2\overline{\mathbf{R}}_0, \overline{\mathbf{P}}_0}{(2\pi\hbar)^M}\langle\chi(\overline{\mathbf{R}}_0, \overline{\mathbf{P}}_0)|\Psi(0)\rangle. \quad (3.1.2)$$

The advantage is that the propagation $e^{-\frac{i}{\hbar}\hat{H}t}|\chi(\overline{\mathbf{R}}_0, \overline{\mathbf{P}}_0)\rangle$ of a Gaussian wave packet $|\chi(\overline{\mathbf{R}}_0, \overline{\mathbf{P}}_0)\rangle$ can be efficiently done on a small compressed basis initially biased to $|\chi(\overline{\mathbf{R}}_0, \overline{\mathbf{P}}_0)\rangle$ as will be described in the Section 3.2. This idea, which is very similar to the semiclassical initial value representation [22–26] (IVR), has been previously used for quantum propagation in Ref. [27] and in the previous version of MCE in Ref. [14]. Therefore, IVR (3.1.2) implements a useful strategy of decomposing a complicated problem into a number of relatively simple tasks, which can be performed in parallel. Although IVR and basis set bias do not constitute any formal approximations, in practice for any finite basis set size N the procedure is accurate only for some time (perhaps rather short), which nevertheless can be sufficient for reproducing the physical properties of the system.

3.2. Swarms of trajectories and coherent state trains

Once the initial wave-function is decomposed into "bits" each of them should be sampled with a basis set and propagated. The use of trajectory swarms and coherent state trains addresses the second problem of creating a basis of overlapping TBFs which stay close to each other. Usually, the initial positions and momenta of TBFs are chosen according to some semi-classical distribution, such as the Wigner function [28] or Husimi Q representation [29]. Such ensembles indeed describe the properties of the initial wave-function. In a multi-dimensional system however, the basis Gaussians selected this way will be very far from each other in phase space, and for any realistic size of a basis set there will be no overlap and interaction between Gaussians even at the initial moment. This does not present a problem in many cases but if we want to move from a semi-classical to a more quantum description, we should use the basis where the TBFs are interacting providing a transfer of quantum amplitudes between them.

The simplest way to create a basis of interacting Gaussians is to use a compressed swarm of trajectories. In this approach, each principal trajectory originating at the centre of the "bit" carries a swarm of satellites, which is placed in its close vicinity providing better sampling and additional flexibility for the wave-function in this part of the phase space. The initial conditions for the principal trajectories are generated as above (i.e. from Husimi or Wigner distribution); the initial conditions for the satellites are taken very close to those for the principal trajectory [13] with random shifts in position and momentum, $\Delta\mathbf{R}$ and $\Delta\mathbf{P}$, generated according to a distribution

$$F(\Delta\mathbf{R}, \Delta\mathbf{P}) \propto \exp\left[-\beta\left(\alpha|\Delta\mathbf{R}|^2 + \frac{1}{4\hbar^2\alpha}|\Delta\mathbf{P}|^2\right)\right], \quad (3.2.1)$$

where β is a compression parameter. The value of β should be carefully optimized for each particular case. The basis is optimal when the overlaps between TBFs in the swarm are in the region of 0.6–0.7. The problem is that, in anharmonic systems, these overlaps will

quickly go down to zero once the TBFs start moving and as soon as the basis Gaussians are no longer coupled to each other the propagation will yield the semi-classical result [29]. Therefore, for smaller values of the parameter β, the basis will be efficient in the beginning, but the interaction between trajectories will disappear it the later times of dynamics. In the opposite case, the basis will be overcomplete in the beginning, as the initial basis functions will be practically indistinguishable. This basis can however become efficient at later times of dynamics as the trajectories run slightly away from each other. Thus, the value of β determines a window in which the swarm basis is optimal.

The basis can be further improved by using coherent state trains [6,12,13], in which additional TBFs are placed along the same trajectory but with a time-shift δt_{train}, as shown in Fig. 1. This greatly expands the basis set at very little computational cost: the most expensive part of on the fly dynamics is electronic structure calculations, and all TBFs in a train are moving along the same trajectory using repeatedly the appropriate electronic structure data, which needs to be calculated only once. An additional advantage of a train basis set is that the interaction between TBFs in the train is preserved during the run.

Expanding the wave function as a sum of "bits" (3.1.2) and propagating each bit independently is not an approximation, but simply a way to exploit the linearity of the Schrödinger equation. Bit-by-bit propagation is accurate only on a short time scale, but the accurate propagation time can be prolonged if the bits are repeatedly branched by reexpanding them according to (3.1.2) into a new swarm basis. However this procedure will rapidly increase the number of bits and the computational cost. In the next section another way of branching the wave function, which is suited to the nonadiabatic dynamics, will be presented.

3.3. Ab initio Multiple cloning algorithm

The Ehrenfest basis set is guided by an average potential, which can be advantageous when quantum transitions are frequent. However, it becomes unphysical in regions of low non-adiabatic coupling when two or more electronic states have significant contributions to the Ehrenfest configuration (1.2): in this case, the difference between the shapes of the potential energy surfaces for different electronic states should lead to branching of the wave packet.

In order to reproduce bifurcations of the wave-function after leaving the non-adiabatic coupling region, we introduced the so called *Ab Initio* Multiple Cloning (AIMC-MCE) [6] algorithm, which was very much inspired by the well-established *Ab Initio* Multiple Spawning (AIMS) [1,30,31]. Cloning addresses the problem of basis misguiding by way of the cloning procedure illustrated in Fig. 1. After a cloning event, an Ehrenfest configuration $|\psi_n\rangle = |\chi_n\rangle \left(\sum_J a_J^{(n)} |\phi_J\rangle \right)$ yields two "clones" of the same configurations:

$$|\psi'_n\rangle = |\chi_n\rangle \left(\frac{a_I^{(n)}}{\left| a_I^{(n)} \right|} \times |\phi_I\rangle + \sum_{J \neq I} 0 \times |\phi_J\rangle \right), \qquad (3.2.2)$$

and

$$|\psi'_{n'}\rangle = |\chi_n\rangle \left(0 \times |\phi_I\rangle + \frac{1}{\sqrt{1 - \left| a_I^{(n)} \right|^2}} \times \sum_{J \neq I} a_J^{(n)} |\phi_J\rangle \right), \qquad (3.2.3)$$

that is, the appropriate basis function is replaced by two basis functions, one of which is now guided by a single potential energy surface, and another by an Ehrenfest force for the remaining electronic states.

The first clone configuration has nonzero amplitudes for only one electronic state, and the second clone contains contributions of all other electronic states. The amplitudes of the two new configurations become:

$$c'_n = c_n \left| a_I^{(n)} \right|, \qquad c'_{n'} = c_n \sqrt{1 - \left| a_I^{(n)} \right|^2}, \qquad (3.2.4)$$

so that the contribution of the two clones $|\psi'_n\rangle$ and $|\psi'_{n'}\rangle$ to the whole wave-function (1.4) remains the same as the contribution of original function:

$$c_n |\psi_n\rangle = c'_n |\psi'_n\rangle + c'_{n'} |\psi'_{n'}\rangle. \qquad (3.2.5)$$

We apply the cloning procedure shortly after a trajectory passes near a conical intersection, when the non-adiabatic coupling is sufficiently low and, at the same time, the so-called breaking force
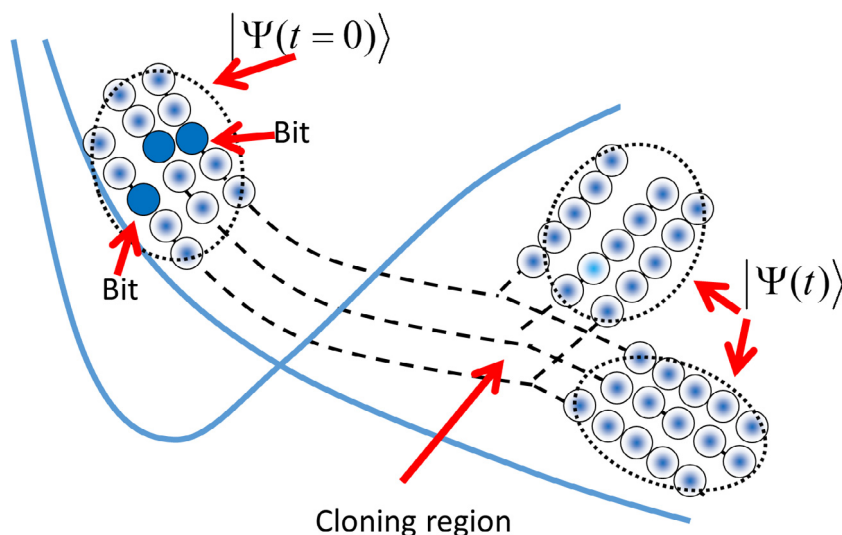

Fig. 1. A sketch of the AIMC-MCE propagation scheme. First the wave-function (encircled by the dotted line) is represented as a superposition of Gaussian Coherent States ("bits" shown by the dark blue circles), each of which is propagated along its trajectory (dotted line). A train basis (light blue) is constructed based on each bit. After passing the intersection the trains bifurcate in the process of cloning. Each bit is actually propagated on a swarm of trains. For simplicity only the central train following the central trajectory is shown without satellite trajectories.

$$\mathbf{F}_I^{(br)} = |a_I|^2 \left(\nabla V_I - \sum_J |a_J|^2 \nabla V_J \right), \tag{3.2.6}$$

which is the force pulling the Ith state away from the remaining states, is sufficiently strong.

The cloning procedure is very much in spirit of the spawning used in the AIMS approach. But, while the AIMS and AIMC-MCE methods have similar computational cost, the advantage of cloning is in exploiting Ehrenfest configurations: in the AIMC-MCE method, the non-adiabatic population transfer between electronic states is possible not only in a small vicinity around conical intersections, as in AIMS, but over the entire relevant phase space. This can be important when conical intersections are not clearly localized. The AIMC-MCE algorithm also does not require any back-propagation of the spawned/cloned basis functions, unlike many [1] (but not all [32,33]) implementations of spawning.

3.4. Tunnelling

The tunnelling of the hydrogen atom can play an important role in many photodynamic processes. As it was mentioned above, all variants of MCE are fully quantum methods because classical trajectories are used only to propagate the basis, while the amplitudes $c_n(t)$ are found by solving time dependent Schrodinger Equation. When Gaussian basis functions are present on either side of the potential barrier, the coupling between them can provide quantum tunnelling through the barrier. In the case of direct *ab initio* dynamics however, the trajectories do not overcome the barrier. A further consideration is that the basis should be kept relatively small. As a result, no basis functions normally would be present on the other side, and they must be placed there "by hand" in order to take tunnelling into account.

Based on the ideas [34,35] previously used in the AIMS method, the algorithm illustrated in Fig. 2 was developed [36] to include tunnelling in AIMC-MCE calculations. We consider here, as an example, the photodissociation of the N—H bond in pyrrole, although this algorithm can be applied to the simulation of any process with a distinctive tunnelling coordinate.

Firstly, the usual AIMC-MCE trajectories are calculated and turning points, where the distance between the hydrogen atom and the radical reaches a local maximum, are identified. Following this, for each of these turning points the shape of the potential barrier is calculated: the length of N—H bond is increased keeping all other degrees of freedom frozen, potential energies are calculated, and the point on the other side of the barrier with the same energy as in the turning point is found. If this point lies farther from the turning point than a set threshold, it is assumed that tunnelling is not possible here, as the potential barrier is too wide. Otherwise, it is used as a starting point for an additional AIMC-MCE trajectory. The new trajectory is calculated both forward and backward in time, and the initial momenta are taken the same as in the turning point ensuring that new trajectories have the same total classical energies as their parent trajectories. This is exactly the procedure used in the multiple spawning approach, thus the method combines cloning for non-adiabatic events and spawning for tunnelling events. The forward propagation of new trajectories often involves branching as a result of cloning; backward propagation is performed without cloning and for a sufficiently short time, until the new and the parent trajectories separate in phase space.

3.5. Solving quantum equations for the amplitudes of Ehrenfest configurations. Post processing

The ideas described above have been implemented in several codes, including *ab initio* direct dynamics programs such as the
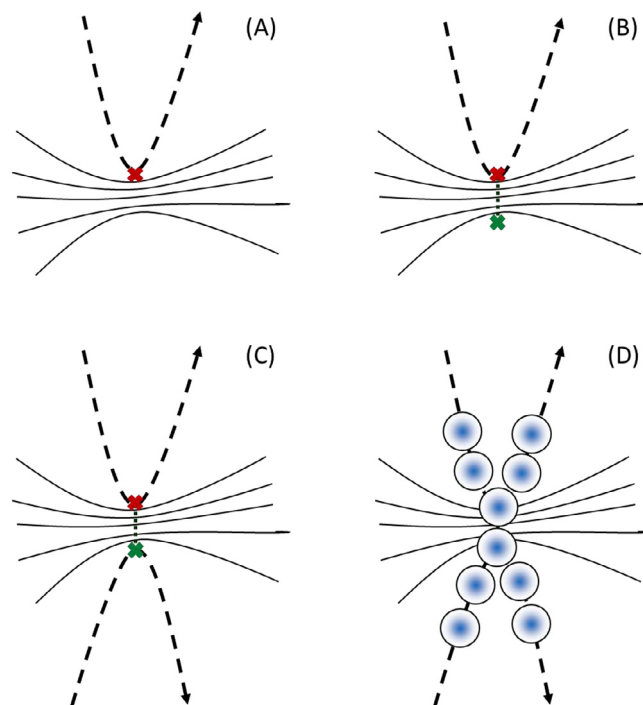

Fig. 2. Illustration of the algorithm used to treat tunnelling in our approach. The set of solid lines represents the barrier, and the dashed lines are the trajectories. (A) Identify turning point (red cross); (B) find a point with the same potential energy on the opposite side of the barrier (green cross); (C) run an additional trajectory through this point; (D) solve the time-dependent Schrodinger Equation in the basis of a coherent state trains moving along the trajectories on both sides of the barrier.

Stanford AIMS code. All implementations of the AIMC-MCE algorithm run a large number of Ehrenfest trajectories independently which are allowed to clone and tunnel creating new branches. At this stage the required total CPU time may reach hundreds of years. Because the trajectories are independent however, all the branches are able to be run in parallel on a large number of processors. When all the trajectories are calculated, we solve Eq. (2.1.18) for quantum amplitudes $c_n(t)$ in a basis of coherent state trains, which have cloned and tunnelled as described above, forming a basis of several trains. The program for solving the equations for $c_n(t)$ simply reads the data accumulated during long and expensive direct dynamics calculations and does not require much CPU time at this stage.

4. Computational results

4.1. Model tests

To verify the sampling techniques described above we report an original set of model tests using the benchmark of the Spin-Boson model, which is a generic paradigmatic model for quantum dissipation, describing a two level (spin ½) system with donor and acceptor states $|\phi_1\rangle$ and $|\phi_2\rangle$ linearly coupled to a bath of harmonic oscillators. The Hamiltonian is given by

$$\hat{H} = \begin{bmatrix} \hat{H}_B + \hat{H}_C + \varepsilon & \Delta \\ \Delta & \hat{H}_B - \hat{H}_C - \varepsilon \end{bmatrix}, \tag{4.1.1}$$

where the bath Hamiltonian H_B and the system-bath coupling Hamiltonian H_C are expressed in mass weighted coordinates as

$$H_B = \sum_j \frac{1}{2}(p_j^2 + \omega_j^2 q_j^2) \tag{4.1.2}$$

$$H_C = \sum_j g_j q_j. \tag{4.1.3}$$

Both the reduced asymmetry parameter, ε, and the coupling parameter between the two spin states, Δ, can be assumed to be constant. The coupling between electronic states and the nuclear bath is given by g_j, which is provided by the bath spectral density

$$J(\omega) = \frac{\pi}{2} \sum_j \frac{g_j^2}{\omega_j} \delta(\omega - \omega_j). \tag{4.1.4}$$

The spin boson model can be used to simulate many different dissipation driven systems, from decoherence in qubits passing through entanglement gates [37] to electron transfer in the condensed phase [38]. The spin boson model is also a very useful test for simulation methods due to its high dimensionality and the comparative simplicity of the Hamiltonian and as such it has been used to test, among others, the path integral method of Makri [39], the method of semiclassical initial value series by Martin-Fierro and Pollak [40], the semiclassical self-consistent approach by Stock [41] and notably the multi-layer multiconfigurational time dependent Hartree (ML-MCTDH) approach by Wang and Thoss [42–44].

As has been already mentioned above, two versions of the MCE method have been developed. The first version, MCEv1, is mostly applied for model systems but the second version, MCEv2, is based on independent Ehrenfest trajectories and is in the core of the direct dynamics via AIMC-MCE approach.

The MCEv1 method was tested [14] against the spin boson model using the Ohmic form of the spectral density with an exponential cutoff, given by

$$J_0(\omega) = \frac{\pi}{2} \alpha_K \omega e^{-\omega/\omega_c}, \tag{4.1.5}$$

where α_K is the so-called Kondo parameter and ω_c is the cutoff frequency. The bath is discretised over N_{dof} degrees of freedom as in ref [45] and as such, the frequencies and coupling coefficients are given by

$$\omega_j = -\omega_c \ln \left[1 - \frac{j}{N_{dof}} (1 - e^{-\omega_m/\omega_c}) \right] \tag{4.1.6}$$

and

$$g_j = \omega_j \sqrt{\frac{\alpha_K \omega_c}{N_{dof}} (1 - e^{-\omega_m/\omega_c})}, \tag{4.1.7}$$

where is the maximal frequency, taken to be $\omega_m = 5\omega_c$. In order to calculate thermally averaged populations, the "bits" (3.1.1) were chosen from a normal distribution sampled with $\sigma_j = \exp[\omega_j/kT] - 1$. Then a swarm of Gaussian basis functions was created for each "bit" by sampling from a normal distribution around its centre (details of this sampling are given in full in ref [14]). To improve convergence, a number of repeat calculations N_{rpt} were carried out by resampling the "bits" and the Gaussian basis functions.

It was shown [14] that the MCEv1 formulation was capable of simulating the spin boson model with very many degrees of freedom accurately, and compared against results gained from the MCTDH simulations of Wang [44] and the ML-MCTDH simulations of Wang and Thoss [42,43]. Using only bit-by-bit propagation and a compressed swarm of basis Gaussians, the MCEv1 approach gave results which were almost indistinguishable from the MCTDH benchmark.

The MCEv2 formulation has been shown to be capable of accurately simulating the short time dynamics of pyrazine, which determines its Franck-Condon spectrum [11,46]. The situation is more complicated however in the case of model systems with high dimensionality and long-time dynamics, such as the spin boson model. The separation of the electronic state coupling and the coupling between the trajectories means that in some systems the MCEv2 basis set does not adequately describe quantum dynamics in phase space, meaning that extra care needs to be taken in constructing and propagating the basis set. This is the case with the spin boson model, as demonstrated in Fig. 3, which compares the results of MCEv2 calculations [47] with the MCTDH benchmark used in the tests for MCEv1. The parameters of calculations using Δ as the unit of energy were the following: for symmetric wells $\hbar\omega_c/\Delta = 2.5$, $\alpha_K = 0.09$, $\Delta/kT = 5.0$, and $\varepsilon/\Delta = 0$ with $N_{dof} = 50$ degrees of freedom; for asymmetric wells $\hbar\omega_c/\Delta = 7.5$, $\alpha_K = 0.10$, $\Delta/kT = 5.0$, and $\varepsilon/\Delta = 1.0$ with $N_{dof} = 50$ degrees of freedom. Fig. 3 (A) shows the population differences calculated using MCEv2 in a basis of trajectory swarms (this method which uses no train basis sets is referred to below as standard MCEv2), using 50 trajectories to construct the swarm in the symmetric case and 200 trajectories to construct the swarm in the asymmetric case. Results were averaged over $N_{rpt} = 256$ repetitions using the same sampling procedure to construct the basis sets as was used for MCEv1 earlier. One can see that the size of the oscillations in the population difference for MCEv2 is large in comparison to those from the MCTDH benchmark for both the symmetric (A I) and asymmetric (A II) cases.

Simple independent Ehrenfest trajectories, used by MCEv2, misguide the basis set. In this particular case the trajectories do not spread out sufficiently, acting as almost a single basis function for both the symmetric and asymmetric cases. By increasing the size of the basis set during propagation through the use of the cloning procedure described in Section 2.3, this can be mitigated. Cloning can however cause the basis set to grow to sizes which make simulation very difficult and time consuming, and so the number of repetitions was reduced to $N_{rpt} = 100$ and a limit was placed on the maximum number of cloning events allowed for each trajectory in the initial swarm. While the imposition of this limit is necessary to ensure that the computational cost of the simulation does not become too cumbersome, it can be implemented without too large an effect on the accuracy of the results due to the fact that the population of a trajectory drops after each bifurcation. This means that a trajectory becomes low-populated after several cloning events making further improvement of sampling by applying additional cloning to this trajectory unpractical. In the case of symmetric wells, the maximum number of cloning events was set to $N_{cln} = 4$ per initial trajectory, as in this case the probability of a cloned trajectory undergoing further cloning events is equal for the trajectories on both states. This being the case, the basis set will grow by a factor of up to $2^{N_{cln}}$ assuming each of the initial trajectories and its subsequent clones undergo the maximum allowed number of cloning events. In the case of the asymmetric spin boson model however more cloning events can be allowed per trajectory, as for this system the wave-function as a whole is decaying onto an acceptor state and so once the cloned basis functions are placed wholly onto the two states the probability of the cloned basis function on the acceptor state undergoing further cloning is negligible; thus it will only be the function placed on the donor state that will experience further cloning events, meaning the basis set will grow instead by up to a factor of $N_{cln} + 1$ As such in this case $N_{cln} = 8$ cloning events are allowed per initial trajectory. Applying cloning to the basis set gives an improved result, as shown in Fig. 3 (B). However in both symmetric and asymmetric cases the oscillations are still too large, meaning that cloning alone does not give a sufficient improvement to the MCEv2 result.

We next look at the impact of using the coherent state trains presented in Section 3.1 to construct our basis. As stated earlier, the use of this approach ensures the preservation of the interaction between basis functions while also greatly increasing the area of
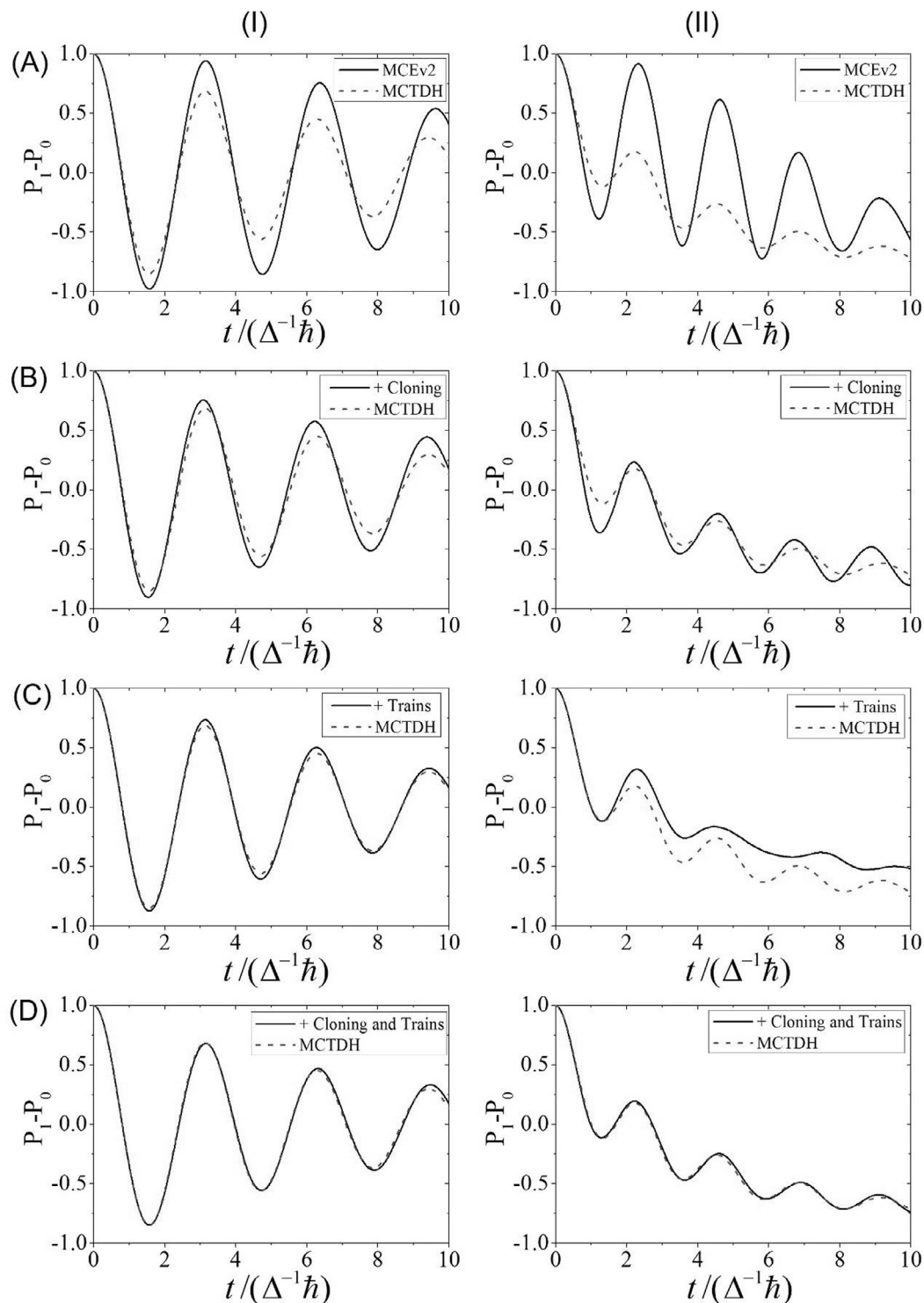
Fig. 3. Comparison of the population differences given by different modifications of the MCE approach for the spin boson model with symmetric (I) and asymmetric (II) wells. All the results are also compared to the numerically exact MCTDH benchmark from ref [42], which is indistinguishable from MCEv1 results [14]. (A) Standard MCEv2. (B) MCEv2 with cloning. (C) MCEv2 with a train-type basis set (D) MCEv2 with cloning and a train-type basis set.

phase space initially covered by the wave-function, and so it is expected that the result would be greatly improved. Trains were constructed as series of 20 TBFs separated by a time displacement of $0.25\Delta^{-1}\hbar$ for the symmetric case and $0.15\Delta^{-1}\hbar$ for the asymmetric case. Swarms of 20 coherent state trains were used giving a total of 400 TBFs in the basis set. The results were averaged over N_{rpt} = 100 repeat calculations. Fig. 3 (C) shows that for the symmet-

ric case the results are almost indistinguishable from the MCTDH results. However for the more difficult asymmetric case there is only agreement over short timescales ($t \approx 1.25 \ \Delta^{-1}\hbar$), with the oscillations greatly dampened as the wave-function decays onto the acceptor state.

Combination of trains with cloning is more successful, yielding a good agreement between the MCEv2 result and that of the

MCTDH benchmark for both the symmetric and asymmetric cases of the spin boson model, as demonstrated in Fig. 3 (D). To deal with the constantly growing basis, the trains here were constructed as a series of only 10 TBFs. Swarms of 10 and 20 coherent state trains were used for symmetric and asymmetric cases respectively, and the restrictions on the number of cloning events were applied as above.

One can see that the results of the MCEv2 calculations in Fig. 3 (D) are practically indistinguishable from those given by MCTDH and thus the accuracy of MCEv2 matches that of MCEv1. This demonstrates that a combination of coherent state trains with cloning is capable of accurately propagating the wave-function for a model system, while each of these basis set improvements may not be sufficient on its own. This conclusion is important because in our *ab initio* direct dynamics calculations we will rely the same sampling techniques verified in this model calculation. A more detailed account of the model calculation can be found in the Ref. [47].

4.2. Direct dynamics calculations

As short time convergence of MCE calculations can be achieved and has been tested on the model systems as described in Section 4.1 above, one can be reasonably confident in the quality of direct dynamics. In this chapter several previously reported *ab initio* direct dynamics "on the fly" MCE simulations are reviewed. The approach was first tested on the calculations of the photodynamics of ethylene after $\pi \rightarrow \pi^*$ excitation [6]. Then, the photodissociation of pyrrole was investigated [7,36]. Finally, to push the limits of the *ab initio* MCE method, simulations were performed of the photodynamics of dendrimer building blocks [19].

The simulation of the dynamics of ethylene and pyrrole was carried out with a modified version of AIMS-MOLPRO [48], which was extended to include Ehrenfest dynamics, using electronic structure data given the complete active space self-consistent field (CASSCF) calculation at SA3-CAS(2,2)/6-31G** and SA4-CAS(8,7)/cc-pVDZ levels of theory respectively. For dendrimers, the MCE-TDDB method was implemented together with the Collective Electron Oscillators (CEO) [49–52] electronic structure code. Excited state energies, gradients and non-adiabatic couplings were calculated on the fly using the Austin Model 1 (AM1) [53] semi-empirical level of theory in combination with the configuration interaction singles (CIS) formalism. This approach has worked well in the previous studies of similar systems [54–56].

The width parameter α of the Gaussian trajectory functions was taken to be 4.7, 22.7 and 19.0 Bohr^{-2} for hydrogen, carbon and nitrogen atoms respectively, as suggested in ref [5]. For MCE and AIMC calculations with train basis sets, each initial TBF generated a single train with a time-shift of about 0.6 fs which corresponds to a nearest neighbour overlap of 0.6–0.7. For the AIMC-MCE simulations, cloning was applied to TBFs when the breaking acceleration of Eq. (3.2.6) exceeded a threshold of 5×10^{-6} a.u. and the norm of the non-adiabatic coupling vector was simultaneously less than 2×10^{-3} a.u. In order to control the growth of the basis set, each TBF was allowed to clone at most 3 times.

Additional computational details can be found in the original works [6,7,19,36].

4.2.1. Initial implementation and test of AIMC-MCE. Photodynamics of ethylene

Ethylene is the most simple molecule with a C=C double bond and has been extensively studied both experimentally and computationally [57–66]. This makes the photodynamics of ethylene an ideal subject for benchmark calculations. We are comparing the results given by the MCE (which refers to *ab initio* MCEv2), AIMC-MCE (i.e. *ab initio* MCEv2 with cloning and train basis sets)

and AIMS methods, including the influence of the use of the coherent state train basis. In all cases, the simulations were restricted to two electronic states, S_0 and S_1, and initiated with 200 distinct initial TBFs, sampled randomly from a Wigner distribution [28] for the ground vibrational state in the harmonic approximation, and then projected onto the S_1 state. This is equivalent to 200 repetitions in the spin-boson simulations described above. The trajectory swarms were not applied here, and the MCE calculations were run in a basis of a single coherent state train. In the case of AIMC-MCE calculations, the size of the basis increased every time that one of TBFs in the train passed through a cloning point, and each of the initial TBFs gave rise to an average of ≈ 4 further TBFs through this process. This is compatible with the basis set growth rate in the AIMS calculations, where each initial condition spawned an average of 4.1 new TBFs.

An example of a wave-function spreading over a train basis set of 200 basis functions is shown in Fig. 4. The initial population is placed on the central TBF of the train. As time progresses, the window of TBFs that are being included in the calculation also shifts forward along the trajectory. Thus, the wave-function stays localized in the middle of the train but gradually spreads over nearby TBFs.

Fig. 5 compares the average ground-state population as a function of time given by several types of calculations: 1) The simple Ehrenfest approach without basis set trains and cloning; 2) MCEv2 with train basis sets; 3) AIMC-MCE method, which is MCEv2 with basis set trains and cloning; 4) *Ab initio* Multiple Spawning (AIMS) benchmark. The ground-state population evolution predicted by the MCE calculations with and without train basis functions is very similar, except that the results are somewhat smoother when the train basis set is used. One can conclude that for this particular problem where the conical intersection is highly peaked (and thus non-adiabatic transitions are both ultrafast and ultra-efficient) the benefits of the train basis set expansion are not very pronounced. As was shown in Section 4.1, the train efficiently smooths out the oscillations in the population, which is not an issue for ethylene.

The initial population dynamics predicted by all methods are similar. However as the ground state population increases, the predictions begin to deviate, and by 100 fs they are quite different. The relaxation rate predicted by AIMC-MCE is significantly faster, and similar to the rate given by AIMS benchmark calculations. This behaviour is as expected: when the population on the ground and excited states are nearly equal, the Ehrenfest dynamics of
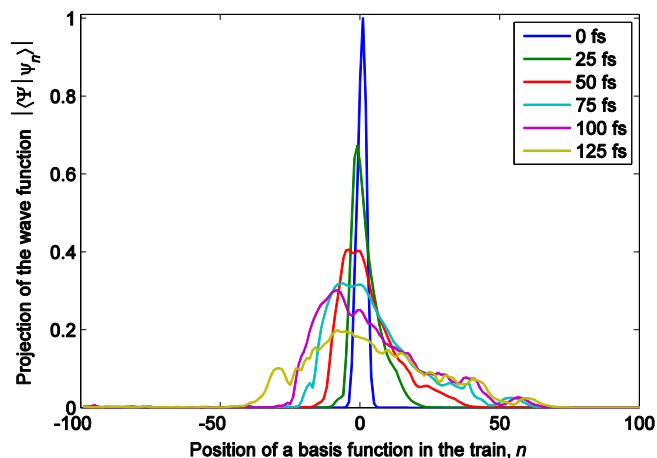

Fig. 4. An example of the spreading of a nuclear part wave-function in a train basis set. The basis is moving along a quasi-classical trajectory so that the maximum of the amplitude remains in the middle of the train. (For interpretation of the references to colour in this figure legend, the reader is referred to the web version of this article.)
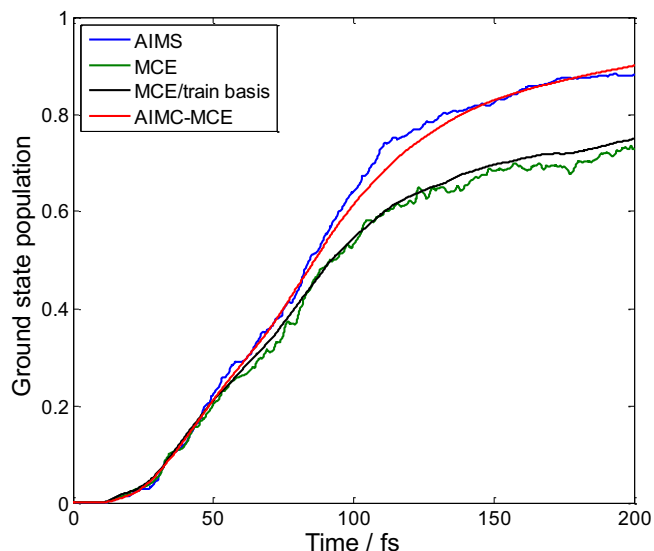
Fig. 5. Calculated ground-state population dynamics of ethylene following $\pi \rightarrow \pi^*$ excitation. Compared are the results obtained using MCE approaches against those given by *Ab Initio* Multiple Spawning (AIMS). Green – simple Ehrenfest dynamics; black – MCE in a coherent state train basis set of 100 TBFs; red – AIMC-MCE; blue – AIMS. The results are averaged over 200 sets of initial conditions. (For interpretation of the references to colour in this figure legend, the reader is referred to the web version of this article.)

the TBFs becomes that of the average of the two electronic states. This will tend to keep the TBFs in the region near the conical intersection longer and population transfer in *both* directions (to the upper state and to the lower state) will be equally probable. This is a manifestation of the violations of detailed balance which are a well-known difficulty in pure Ehrenfest dynamics [67,68]. The cloning procedure in AIMC-MCE solves this problem by allowing the TBFs to separate and evolve on adiabatic states.

4.2.2. Photodissociation of pyrrole with AIMC-MCE

Photodynamics of pyrrole is an important prototype for a number of biologically relevant photochemical processes. For example, light harvesting in plants, fluorescence of living organisms, and visual reception all involve photochemical reactions that include electronic excitation and subsequent electronically non-adiabatic dynamics. Recently, significant progress has been made in experimental ultrafast time resolved spectroscopy studies of various photochemical reactions, focused on biologically related molecules. The derivatives of heteroaromatic molecules such as pyrrole, imidazole, and phenol are important chromophores of many biologically relevant molecules. The mechanisms of their photochemistry have been a focus of experimental [69–71] and theoretical [72–79] attention. It was suggested that the N—H/O—H bond fission was an important channel in the photodissociation dynamics, and the role of the $^1\pi\sigma*$ states in this process has been emphasized [80–88].

The AIMC-MCE approach was applied [7,36] to simulate the dynamics of pyrrole following excitation to the first excited state. In particular, the total kinetic energy release (TKER) spectra and velocity map images (VMI) were calculated. The TKER and VMI measurements can provide invaluable information on the dynamics of various bond fission reactions, but their numerical calculation is a difficult task because they reflect important details of quantum dynamics in multidimensional systems, where realistic calculations beyond simple reduced dimensionality models are challenging.

The calculations were run both with and without taking tunnelling into account. Three electronic states were taken into consideration during the dynamics – the ground state and the two lowest singlet excited states. The initial Ehrenfest configurations were randomly sampled from the ground state vibrational Wigner distribution [28] in the harmonic approximation. The transition from the ground to the first excited state is symmetry-forbidden in the Franck-Condon approximation and only occurs due to the coordinate-dependence of the transition dipole moment. The photoexcitation was approximated by simply lifting the ground state wavepacket to the excited state, as would be appropriate for an instantaneous excitation pulse within the Condon approximation. Of course, the details of the initial photoexcited wavepacket are not completely accounted for in this approximation (which assumes the transition dipole moment for the transition is finite and independent on nuclear coordinates). Although we expect the simplest model of the initial wave packet to be qualitatively correct, we are working on more rigorous and accurate ways to treat initial excitation, which would be able to account for the shape of the pump pulse.

Initially 900 non-interacting AIMC trajectories were run for 200 fs or until the dissociation occurred, defined as an N—H distance exceeding 4.0 Å. For a small number of trajectories, simulations exhibiting N—H dissociation were carried out to the full 200 fs in order to investigate the dynamics of the radical. For all initial trajectories, as well as for their branches resulting from cloning, the turning points for the N—H bond length were identified and the widths of the potential barrier were calculated. Additional trajectories on the other side of the barrier were placed if the width of the barrier did not exceed 0.5 Bohr, which corresponds to an overlap of ~0.3 between Gaussian basis functions. The new trajectories were propagated backward for 20 fs to accommodate the train basis set, and forward until dissociation occurred or until the trajectory time exceeded 200 fs.

For each initial trajectory with all its branches and tunnelling sub-trajectories, Eq. (2.1.18) was solved using train basis set of $N = 21$ Gaussians per branch. The total size of the basis was constantly changing because of the inclusion of new branches. The final amplitudes c_n provided statistical weights for each of the branches, which were used in the analysis that follows.

As a result of cloning, 900 initial configurations gave rise to 1131 trajectory branches. This corresponds to an average of ~0.25 cloning events per initial trajectory. For these branches, 7702 local maxima of N—H bond length were found, of which 2376 have been identified as possible tunnelling points. For all these points, the sub-trajectories were run, which finally gave 3203 additional branches, 4334 branches in total. The majority of these branches underwent N—H dissociation within our computational time of 200 fs: the total statistical weight of dissociative trajectories was 92%, of which 53% is the contribution of tunnelling sub-trajectories.

The calculated kinetic energy distribution of the ejected hydrogen atom is presented in Fig. 6 together with the experimental TKER spectrum [69]. Both distributions clearly exhibit two contributions: a large peak at higher energies, and a small contribution at lower energies. One can see that adapting the basis set to tunnelling leads to a significant increase in the dissociation yield in the low/middle-energy region of the spectrum. After the renormalization, this increase shifts the high-energy peak of TKER spectrum toward the lower energies by about ~ 1000 cm^{-1} and makes the low-energy peak slightly more pronounced. While the calculated energies are still on average about 1.5 times higher than experimental values, this difference can be ascribed to the lack of dynamic electron correlation in the CASSCF approach. The comparison of CASSCF and MS-CASPT2 energies for pyrrole indicates [7] that the use of more accurate MS-CASPT2 potential energy surfaces

would lead to a shift in the kinetic energy peak of ~1800–1900 cm^{-1} towards lower energies, significantly improving the agreement with experimental results.

Analysis of the electronic state amplitudes in the Ehrenfest configurations (1.2) shows that the bifurcation of the wave-function while passing through a conical intersection plays an important role in the formation of a two-peak spectrum: the high kinetic energy product is predominantly in the ground state, while the low energy peak is formed by mostly low-weight branches with substantial contribution from excited electronic states. Fig. 7 presents an example of such a bifurcating trajectory. At about 55 fs after photoexcitation, this trajectory reaches an intersection for the first time. After passing the intersection, the ground and first excited states of the original TBF are approximately equally populated, so the cloning procedure is applied creating instead two TBFs, one in the ground state and one in the excited. At this point, the potential energy surfaces for ground and excited states have opposite gradients. This leads to the acceleration of the hydrogen

atom for the TBF associated with ground state and, at the same time, slows it down for excited state TBF. As a result, although both branches lead to dissociation, the kinetic energies of ejected atoms are significantly different: the ground state branch contributes to the high energy peak of the distribution in Fig. 7, while the excited state branch contributes to the low energy peak. For the ground state branch, the remaining vibrational energy of the radical is low, so it remains in the ground state for the rest of the run and does not reach the intersection again. For the excited state branch, the energy taken away by the hydrogen atom is lower leaving the pyrrolyl radical with sufficient energy to pass through numerous intersections with population transfer between the ground and both excited states. Naturally, quenching to the ground state will happen eventually for this branch but the time scale of this process is much longer than that for the dissociation, while the TKER spectrum is only affected by the radical dynamics until the H atom is lost.

In order to calculate the velocity map image with respect to the laser pulse polarization, we must average the velocity distribution of hydrogen atoms relative to the axes of the molecule, over all possible orientations of the molecule:

$$I(r, \varphi) \propto \delta(r - |\mathbf{v}|) \int \int \int d\alpha \, d\beta \, d\gamma \cos^2\left(\xi(\alpha, \beta, \gamma)\right) \delta(\varphi - \phi(\theta, \alpha, \beta, \gamma)),$$

(4.2.1)

where α, β and γ are Euler angles, θ is the angle between the atom velocity vector $\mathbf{v}$ and the transition dipole of the molecule, $\xi(\alpha, \beta, \gamma)$ is the angle between the transition dipole and light polarization vectors, and $\phi(\theta, \alpha, \beta, \gamma)$ is the angle between the light polarization
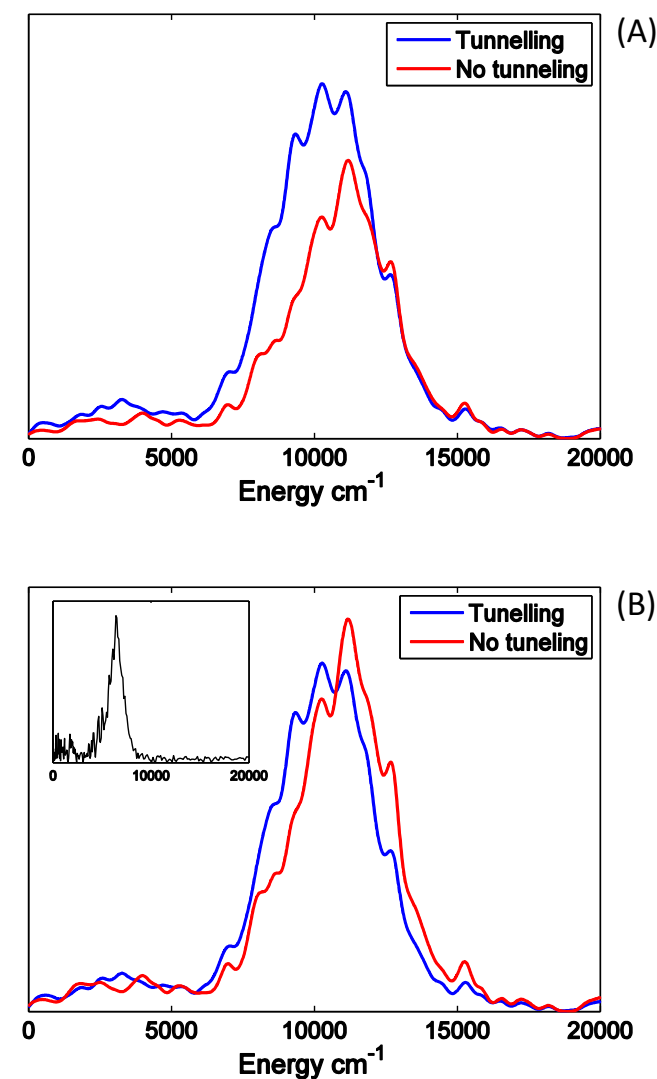

Fig. 6. Total kinetic energy release (TKER) spectrum for the photodissociation of pyrrole calculated with (blue) and without (red) taking tunnelling into account. Both spectra are averaged over the same ensemble of initial configurations and smoothed by replacing delta-functions with Gaussian functions ($\sigma = 200$ cm^{-1}). Part (A) presents the spectra before normalization showing an increase of the yield in the low- and middle-energy regions. Part (B) presents the same spectra after the normalization, and the inset shows the experimentally measured spectrum [69]. (For interpretation of the references to colour in this figure legend, the reader is referred to the web version of this article.)
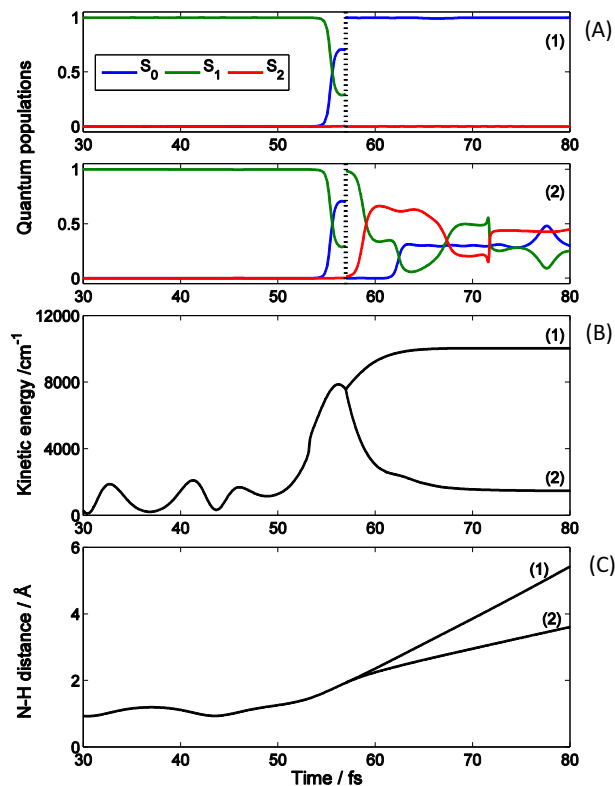

Fig. 7. An example of trajectory bifurcation at a conical intersection in the simulations of the photodissociation of pyrrole. Electronic state populations (A), the kinetic energy of H atom (B) and N_H distance (C) as a function of time. Fast and slow branches are referred as (1) and (2) respectively. Dotted vertical line indicates the moment when cloning was applied. (For interpretation of the references to colour in this figure legend, the reader is referred to the web version of this article.)

vector and atom velocity. Here we take into account that the probability of excitation is proportional to $\cos^2(\xi)$. Integrating over Euler angles and replacing, as usual, the δ-function for |**v**| with a narrow Gaussian function, we obtain:

$$I(r, \varphi) \propto \exp\left(-\frac{(r - |\mathbf{v}|)^2}{2\sigma^2}\right)\left(\cos^2(\theta)\cos^2(\varphi) + \frac{1}{2}\sin^2(\theta)\sin^2(\varphi)\right).$$

(4.2.2)

Fig. 8 shows the simulated velocity map with respect to the laser pulse polarization assuming that the transition dipole is normal to the molecular plane. The simulations reproduce the main feature of the experimental [69] velocity map image, which is the anisotropy of the intense high energy part. The results are also consistent with experiment in the low energy region showing an isotropic distribution, although admittedly the statistics of both experiment and simulation are poorer in the region of low energy.

In the AIMC-MCE simulation of the photodynamics of ethylene and pyrrole described in the above sections, all electrons and all nuclei were treated on a fully quantum basis. The number of basis functions was comparable with that used in the model simulations in Section 4.1, and similar sampling techniques (i.e. cloning, trains and bit-by-bit propagation) were used to improve convergence. Thus, these calculations represent an example of a fully quantum treatment of non-adiabatic dynamics in polyatomic molecules.

4.2.3. Excitation dynamics in dendrimers with ab initio MCE-TDDB

Dendrimers are highly branched conjugated macromolecules which possess well-defined regular structures with numerous peripheral groups, branched repeat units, and a core. Each of these components acts as individual chromophore units absorbing light at different ranges of the spectrum [89]. The π-conjugation in the regular arrays of such coupled chromophore units provides an efficient and controllable unidirectional energy transfer in dendrimers [49].

The time evolution of electronic excitations in organic conjugated materials is determined by non-adiabatic dynamics involving multiple coupled electronic excited states. Following photoexcitation, multiple pathways to electronic and vibrational relaxation arise which involve energy and/or charge transfer, internal conversion, and transition density localization/delocalization. A large number of electronic states and intersections between them makes dendrimers and other large conjugated molecules a nearly ideal object for Ehrenfest based approaches: a wave packet undergoes frequent transition between many coupled electronic states and, as a result, its motions can be well described by a mean-field Ehrenfest trajectory. Electronic states can however change very sharply in large conjugated molecules, in particular as a result of the change in the energy order for the states localized on spatially separated moieties. Such changes, known as trivial unavoided crossings [18], can frequently occur for molecules composed of multiple chromophore units, such as dendrimers.

The MCE-TDDB method has been developed specifically to treat such systems. It was applied [19] to simulations of the excited state dynamics of a system composed of two- and three-ring linear polyphenylene ethynylene (PPE) chromophore units linked through a meta-substitution, as shown in Fig. 9. These chromophore units correspond to building blocks of more complex phenylethynylperylene-terminated dendrimers, such as the nanostar [49,90–93]. The figure shows that the excited states S_1 and S_2 are localized on different linear fragments. The non-adiabatic couplings between these fragments are responsible for quantum transition from the S_2 to S_1 state resulting in the two-ring → three ring unidirectional electronic energy flow. Thus, this system is a good model for analysing intramolecular electronic and vibrational energy transfer between chromophore units.
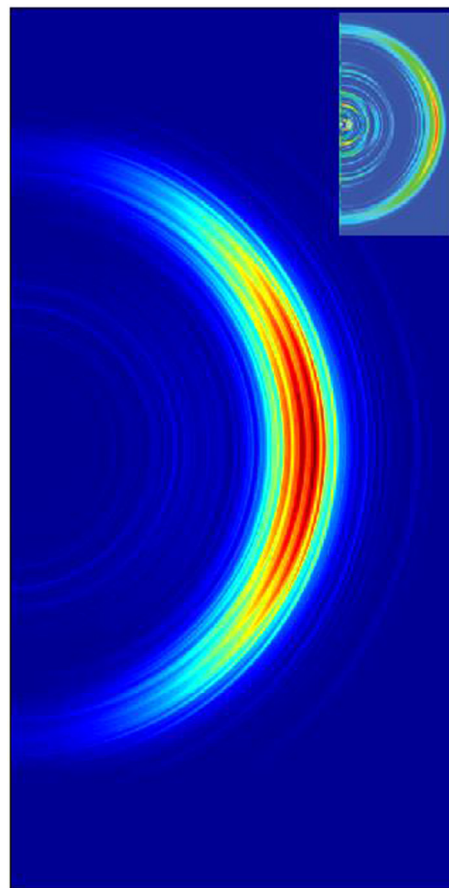

Fig. 8. Simulated velocity map image (VMI) for the photodissociation of pyrrole assuming that the transition dipole moment is normal to the molecule plane. The experimental VMI [69] is shown in the inset.

Six singlet electronic states (S_1-S_6) were included in the simulations, and the excited-state trajectories of 150 fs duration were propagated at constant energy with a 0.02 fs time step. In order to generate the initial conditions for excited-state dynamics, 1 ns of ground state molecular dynamics at 300 K was first performed with 0.5 fs time step using a Langevin friction coefficient γ of 2.0 ps^{-1}. Snapshots of nuclei positions and momenta (conformational phase space) have been collected and used as initial conditions for the subsequent photoexcitation dynamics modelling. The excited-state trajectories have been started from these initial configurations by instantaneously promoting the system to the state I selected according to a Frank-Condon window:

$$g_I(\mathbf{R}) = f_I \exp[-T^2(\Omega_{\text{laser}} - \Omega_I(\mathbf{R}))]^2,$$

where Ω_{laser} is the frequency of the laser pulse, $\Omega_I(\mathbf{R})$ and f_I are the transition energy and normalized oscillator strength of the Ith excited state respectively. The pulse is centred at 348 nm (the maximum of the absorption spectrum for the state S_2) and assumed to have a Gaussian shape $f(t) \propto \exp(-t^2/2T^2)$ with $T = 42.5$ fs corresponding to a FWHM (Full Width at Half Maximum) of 100 fs.

The MCE-TDDB simulations were performed for 100 trajectory swarms consisting of 10 trajectories each: the principle one and 9 satellites. The initial conditions for satellites were generated according to Eq. (3.2.1) with β=1000, which corresponds to the initial overlap of about 0.93 between the principle and satellite trajectories. For each trajectory in a swarm, the coherent state train basis of 11 basis functions was used. The results were compared with those given by the NA-ESMD (non-adiabatic excited-state
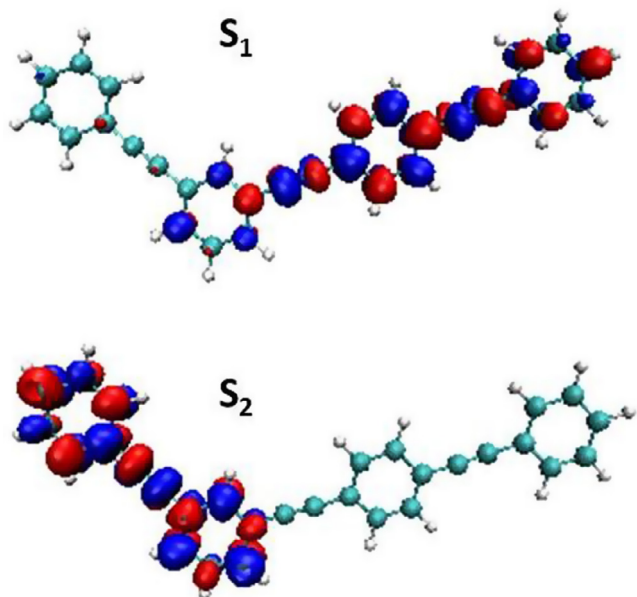
Fig. 9. Model dendritic molecule, which involves two- and three-ring linear poly (phenylene ehynylene) units linked by meta-substitution. The figure shows the initial localization of the electronic excitation for the two lowest excited states.

molecular dynamics) surface hopping method [94,95], which is based on Tully's fewest-switches (FSSH) algorithm [96–98]. The NA-ESMD calculations were performed for a sets of 100 excited-state trajectories with the same initial conditions as for principal trajectories in MCE-TDDB calculations.

Fig. 10 presents the average populations of the lowest four electronic states as a function of time calculated using the MCE-TDDB method, and their comparison with the results given by NA-ESMD surface hopping with and without the instantaneous decoherence corrections [99]. One can see that although all three dependencies are generally similar, the rates of $S_2 \rightarrow S_1$ relaxation are sufficiently different, and the rate given by the MCE calculations is in between two limiting cases of surface hopping with and without decoherence corrections. This can be an indication that the MCE approach naturally accounts for decoherence and, unlike surface hopping, do not require any additional *ad hoc* corrections. More details can be found in Ref. [19]. MCE-TDDB can also be systematically improved. In particular, no cloning was allowed in our simulation, as we assumed that the Ehrenfest approach should be adequate for a system with multiple crossings. This, however, should be verified and we are working on introducing an efficient cloning algorithm here.

5. Summary and future prospects

In this paper we review the Multiconfigurational Ehrenfest method as a technique to simulate quantum multidimensional systems. MCE uses Ehrenfest trajectories to guide the basis of Gaussian Coherent States to simulate electronically non-adiabatic dynamics, treating nuclear degrees of freedom also on a fully quantum level. Two versions, MCEv1 and MCEv2, have been developed. The MCEv1 method, which uses interacting trajectories that "push" each other, is an efficient technique to simulate model systems, however it is not well suited to the case of direct dynamics. This being the case, the MCEv2 method has been developed which uses independent Ehrenfest trajectories. While such trajectories misguide the basis somewhat, this can be corrected, and a number of sampling techniques, such as "bit-by-bit" propagation, swarms and train basis sets, basis tunnelling, and trajectory cloning, have been developed by us in order to address this issue. These tech-
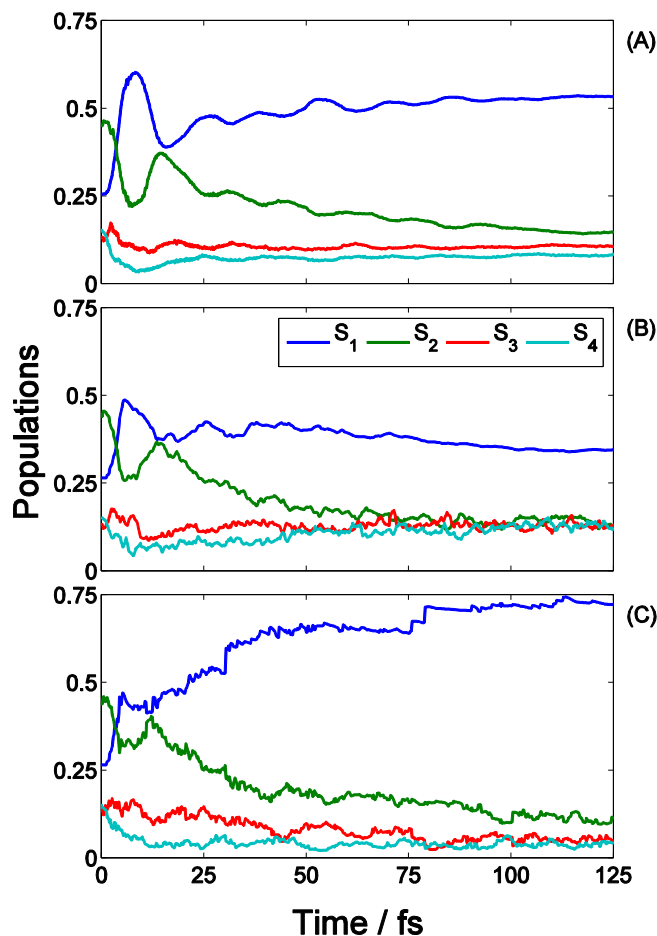

Fig. 10. Calculated dynamics of the model dendritic molecule shown in Fig. 9 following its photoexcitation. Average populations of the four lowest electronic states as a function of time. The figure shows the results of MCE calculations (A) and two limiting cases of surface hopping: NA-ESMD without (B) and with (C) decoherence corrections [99]. (For interpretation of the references to colour in this figure legend, the reader is referred to the web version of this article.)

niques have been tested for the spin-boson model and it has been shown that MCEv2 converges to the exact result. A direct dynamics *Ab initio* Multiple Cloning algorithm has been developed, which performs fully quantum MCEv2 simulations "on the fly" using the sampling techniques proven by applications to model systems. In addition to good sampling methods we have used interpolations for nondiagonal coupling matrix elements that do not need any additional information and new electronic structure calculations. As a result, a large ensemble of Ehrenfest trajectories can be run independently and solving the equations which couple the basis configurations can be done later as a "post processing". We have performed a number of direct dynamics simulations which treat both electrons and nuclei on a fully quantum level, albeit on a short time scale of several hundred femtoseconds.

Several new projects are now in progress and will be reported later

1) AIMC-MCE will be systematically applied to simulate ultra-fast electronically non-adiabatic dynamics of hydrogen photodetachment in small aromatic molecules, such as pyrrole and azoles (imidazole, pyrazole *etc*), and in larger biomolecule analogues (e.g. nucleobases and amino acids) such as indoles, phenols and thiophenols [80–82,85,100–103], which are important because they serve as building blocks of larger biomolecules. For example, it is believed that

hydrogen photodetachment plays an important role in the photostability of proteins [104]. The photodynamics of aromatic molecules has been studied experimentally by imaging techniques pioneered by M. Ashfold [80–88,100–103,105–110], and AIMC-MCE simulations can help to reach a better understanding of the mechanisms of hydrogen photodetachment. Advantage will be taken of the fact that AIMC-MCE theory is extremely well suited for comparison with present gas phase time resolved imaging experiments [69,107,110–118]. Both theory [6,7,9,10] and experiments [69,107,110–118] probe the evolution of an initially localized quantum wave packet on the sub-picosecond time scale.

2) The AIMC-MCE method will also be applied to simulations of hydrogen photodetachment in condensed phase pump-probe experiments. By comparing the dynamics of hydrogen photodetachment in gas and condensed phase, we will verify the recent hypothesis that the dynamics in solution are often similar to those in the gas phase on ultrafast timescales [119–121].

3) We are now working on the implementation of the cloning algorithm for MCE-TDDB calculations involving a large number of electronic states aiming at simulations of the photodynamics in large conjugated molecules. Along with direct dynamics, the MCE approach will be applied to models, such as Frenkel-Holstein and Pariser–Parr–Pople, which are commonly used in the theoretical study of excitations in conjugated polymers (see, e.g., Refs. [122–126]).

4) The AIMC-MCE method has already been applied [127] to simulations of emerging ultrafast time resolved X-ray scattering experiments [128], which became possible with the appearance of new powerful light sources and synchronizing X-ray scattering probes with a femtosecond laser pumps. Time resolved X-ray experiments allow one to observe images of a molecule in motion frame by frame with a femtosecond time scale resolution between laser pump and X-ray probe pulses. More work is in progress to expand these ideas.

The MCE method for model systems has been implemented in several codes in our group. Its direct dynamics MCE/AIMC-MCE and MCE-TDDB versions were implemented together with AIMS and CEO packages respectively. The formalism itself is quite straightforward and we hope that this review can help other groups to use similar ideas alongside with other trajectory based techniques of simulations of ultrafast photoprocesses.

Appendix A. Ehrenfest force in adiabatic basis or TDD basis

In order to derive Eq. (2.2.8) for the Ehrenfest force in an adiabatic basis, let us rewrite the Eq. (2.1.11) for the force as

$$\mathbf{F}_n = \left\langle \phi_n \left| -\frac{d}{d\overline{\mathbf{R}}_n} \hat{V}(\overline{\mathbf{R}}_n) \right| \phi_n \right\rangle, \tag{A1.1}$$

where $|\phi_n\rangle$ is the electronic part of nth basis function (see (1.2)). Here we use the fact that diabatic wave-functions $|\phi_I\rangle$ in (2.1.11) do not depend on $\mathbf{R}$, and apply the approximation similar to (2.2.2), replacing the averaging over χ_n by the operator $\hat{V}(\overline{\mathbf{R}}_n)$ for the centre of Gaussian:

$$\left\langle \chi_n \phi_I \left| \hat{V} \right| \phi_J \chi_n \right\rangle \approx \left\langle \phi_I \left| \hat{V}(\overline{\mathbf{R}}_n) \right| \phi_J \right\rangle, \tag{A1.2}$$

Eq. (A1.1), which represents a particular case of the Hellman-Feynman theorem [129,130], is valid in both diabatic and adiabatic basis sets; the force here is written as an expectation value of an operator regardless of a particular representation of electronic wave-functions $|\phi_n\rangle$. Thus, we can rewrite Eq. (A1.1) representing $|\phi_n\rangle$ in the basis $|\phi_I(\overline{\mathbf{R}}_n)\rangle$:

$$\mathbf{F}_n = -\sum_{I,J} a_I^{(n)*} a_J^{(n)} \left\langle \phi_I(\overline{\mathbf{R}}_n) \left| \frac{d}{d\overline{\mathbf{R}}_n} \hat{V}(\overline{\mathbf{R}}_n) \right| \phi_J(\overline{\mathbf{R}}_n) \right\rangle. \tag{A1.3}$$

Taking into account that $|\phi_I(\overline{\mathbf{R}}_n)\rangle$ are the eigenfunctions of the operator $\hat{V}(\overline{\mathbf{R}}_n)$, we get

$$\frac{d}{d\overline{\mathbf{R}}_n} \left\langle \phi_I(\overline{\mathbf{R}}_n) \left| \hat{V}(\overline{\mathbf{R}}_n) \right| \phi_J(\overline{\mathbf{R}}_n) \right\rangle = \frac{d}{d\overline{\mathbf{R}}_n} V_I(\overline{\mathbf{R}}_n) \delta_{IJ} \tag{A1.4}$$

and

$$\begin{aligned}
\frac{d}{d\overline{\mathbf{R}}_n} \langle \phi_I(\overline{\mathbf{R}}_n)|\hat{V}(\overline{\mathbf{R}}_n)|\phi_J(\overline{\mathbf{R}}_n)\rangle &= \left\langle \phi_I(\overline{\mathbf{R}}_n) \left| \frac{d}{d\overline{\mathbf{R}}_n} \hat{V}(\overline{\mathbf{R}}_n) \right| \phi_J(\overline{\mathbf{R}}_n) \right\rangle \\
&+ \left\langle \frac{d}{d\overline{\mathbf{R}}_n} \phi_I(\overline{\mathbf{R}}_n) \middle| \phi_J(\overline{\mathbf{R}}_n) \right\rangle V_J(\overline{\mathbf{R}}_n) \\
&+ \left\langle \phi_I(\overline{\mathbf{R}}_n) \left| \frac{d}{d\overline{\mathbf{R}}_n} \phi_J(\overline{\mathbf{R}}_n) \right\rangle V_I(\overline{\mathbf{R}}_n).
\end{aligned} \tag{A1.5}$$

Then comparing these two equations, we obtain:

$$\begin{aligned}
\left\langle \phi_I(\overline{\mathbf{R}}_n) \left| \frac{d}{d\overline{\mathbf{R}}_n} \hat{V}(\overline{\mathbf{R}}_n) \right| \phi_I(\overline{\mathbf{R}}_n) \right\rangle &= \frac{d}{d\overline{\mathbf{R}}_n} V_I(\overline{\mathbf{R}}_n) \delta_{IJ} \\
&- \left\langle \frac{d}{d\overline{\mathbf{R}}_n} \phi_I(\overline{\mathbf{R}}_n) \middle| \phi_J(\overline{\mathbf{R}}_n) \right\rangle V_J(\overline{\mathbf{R}}_n) \\
&- \left\langle \phi_I(\overline{\mathbf{R}}_n) \left| \frac{d}{d\overline{\mathbf{R}}_n} \phi_J(\overline{\mathbf{R}}_n) \right\rangle V_I(\overline{\mathbf{R}}_n).
\end{aligned} \tag{A1.6}$$

Substituting (A1.6) into (A1.3) and taking into account that NACMEs (2.2.5) are anti-symmetric $\left(\mathbf{d}_{IJ}^{(n)} = -\mathbf{d}_{JI}^{(n)} \right)$, we come to the Eq. (2.1.7) for the Ehrenfest force in an adiabatic or TTD basis:

$$\mathbf{F}_n = -\sum_I a_I^{(n)*} a_I^{(n)} \frac{d}{d\overline{\mathbf{R}}_n} V_I(\overline{\mathbf{R}}_n) + \sum_{I\neq J} a_I^{(n)*} a_J^{(n)} \mathbf{d}_{IJ}^{(n)} \left(V_I(\overline{\mathbf{R}}_n) - V_J(\overline{\mathbf{R}}_n) \right). \tag{A1.7}$$

A.2. The evolution of Ehrenfest amplitudes in TDD basis

Taking into account that the overlaps in TDD representation include both nuclear and electronic parts, Eq. (2.1.12) for the time-evolution of amplitudes takes the form

$$\dot{a}_I^{(n)} = \sum_J \left(-\frac{i}{\hbar} \left\langle \chi_n \phi_I \left| \hat{H} \right| \chi_n \phi_J \right\rangle - \left\langle \phi_I^{(n)} \left| \frac{\partial \phi_J^{(n)}}{\partial t} \right. \right\rangle \right) a_J^{(n)} - \left\langle \chi_n \left| \frac{\partial \chi_n}{\partial t} \right. \right\rangle a_I^{(n)}.$$

(A2.1)

Then, substituting

$$\left\langle \phi_I^{(n)} \left| \frac{d\phi_J^{(n)}}{dt} \right. \right\rangle = \dot{\mathbf{R}}_n \mathbf{d}_{IJ}^{(n)}$$

(A2.2)

and using, as before, (2.1.16) and approximation (2.2.2), we get

$$\dot{a}_I^{(n)} = -\frac{i}{\hbar} V_I a_I^{(n)} - \sum_J \dot{\mathbf{R}}_n \mathbf{d}_{IJ}^{(n)} a_J^{(n)}.$$

(A2.3)

Taking into account that $\dot{\mathbf{R}}_n = \overline{\mathbf{P}}_n / \mathbf{M}$, one can see that Eq. (A2.3) is exactly the same as Eq. (2.1.8) with effective Hamiltonian (2.1.9).

A.3. The approximation of matrix elements in TDDB

First, we insert the unity $\sum_K |\phi_K(\mathbf{R})\rangle\langle\phi_K(\mathbf{R})| = 1$ into the matrix elements between electronic states belonging to different Ehrenfest configurations:

$$\left\langle \phi_I^{(m)} \left| \hat{V}(\mathbf{R}) \right| \phi_J^{(n)} \right\rangle = \sum_{K,L} \left\langle \phi_I^{(m)} \middle| \phi_K(\mathbf{R}) \right\rangle \left\langle \phi_K(\mathbf{R}) \left| \hat{V}(\mathbf{R}) \right| \phi_L(\mathbf{R}) \right\rangle \left\langle \phi_L(\mathbf{R}) \middle| \phi_J^{(n)} \right\rangle$$
$$= \sum_K \left\langle \phi_I^{(m)} \middle| \phi_K(\mathbf{R}) \right\rangle V_K(\mathbf{R}) \left\langle \phi_K(\mathbf{R}) \middle| \phi_J^{(n)} \right\rangle,$$

(A3.1)

where $|\phi_K(\mathbf{R})\rangle$ are adiabatic electronic eigenfunctions. Now, similar to the case of an adiabatic basis, using the first-order BAT expansion we can approximate the potential energy matrix elements as:

$$\left\langle \chi_m \phi_I^{(m)} \left| \hat{V}(\mathbf{R}) \right| \chi_n \phi_J^{(n)} \right\rangle \approx \frac{1}{2} \left\langle \chi_m \left| \sum_K \left\{ \left\langle \phi_I^{(m)} \middle| \phi_K^{(m)} \right\rangle V_K(\overline{\mathbf{R}}_m) \left\langle \phi_K^{(m)} \middle| \phi_J^{(n)} \right\rangle \right. \right. \right.$$
$$+ (\mathbf{R} - \overline{\mathbf{R}}_m) \frac{d}{d\mathbf{R}} \left\langle \phi_I^{(m)} \middle| \phi_K(\mathbf{R}) \right\rangle V_K(\mathbf{R}) \left\langle \phi_K(\mathbf{R}) \middle| \phi_J^{(n)} \right\rangle |_{\mathbf{R}=\overline{\mathbf{R}}_m}$$
$$+ \left\langle \phi_I^{(m)} \middle| \phi_K^{(n)} \right\rangle V_K(\overline{\mathbf{R}}_n) \left\langle \phi_K^{(n)} \middle| \phi_J^{(n)} \right\rangle$$
$$\left. \left. + (\mathbf{R} - \overline{\mathbf{R}}_n) \frac{d}{d\mathbf{R}} \left\langle \phi_I^{(m)} \middle| \phi_K(\mathbf{R}) \right\rangle V_K(\mathbf{R}) \left\langle \phi_K(\mathbf{R}) \middle| \phi_J^{(n)} \right\rangle |_{\mathbf{R}=\overline{\mathbf{R}}_n} \right\} \middle| \chi_n \right\rangle$$
$$\approx \frac{1}{2} \left\langle \phi_I^{(m)} \middle| \phi_J^{(n)} \right\rangle \left\{ \left\langle \chi_m \middle| \chi_n \right\rangle \left[V_I(\overline{\mathbf{R}}_m) + V_J(\overline{\mathbf{R}}_n) \right] \right.$$
$$\left. + \frac{1}{2} \left\langle \chi_m \left| \left[(\mathbf{R} - \overline{\mathbf{R}}_m) \cdot \frac{d}{d\overline{\mathbf{R}}_m} V_I(\overline{\mathbf{R}}_m) \right] + \left[(\mathbf{R} - \overline{\mathbf{R}}_n) \cdot \frac{d}{d\overline{\mathbf{R}}_n} V_J(\overline{\mathbf{R}}_n) \right] \middle| \chi_n \right\rangle \right\}$$

(A3.2)

In addition to the matrix elements of the Hamiltonian, Eq. (2.1.18) for the time-evolution of amplitudes c_n also includes term $\langle \psi_m(t) | \frac{d}{dt} | \psi_n(t)\rangle$, which has the following form in a TDD basis:

$$\left\langle \psi_m \left| \frac{d\psi_n}{dt} \right. \right\rangle = \left\langle \chi_m \left| \frac{d\chi_n}{dt} \right. \right\rangle \sum_{I,J} \left\langle \phi_I^{(m)} \middle| \phi_J^{(n)} \right\rangle \left(a_I^{(m)} \right)^* a_J^{(n)}$$
$$+ \langle \chi_m | \chi_n \rangle \sum_{I,J} \left\langle \phi_I^{(m)} \middle| \phi_J^{(n)} \right\rangle \left(a_I^{(m)} \right)^* \dot{a}_J^{(n)}$$
$$+ \langle \chi_m | \chi_n \rangle \sum_{I,J} \left\langle \phi_I^{(m)} \left| \frac{d\phi_J^{(n)}}{dt} \right. \right\rangle \left(a_I^{(m)} \right)^* a_J^{(n)}$$

(A3.3)

where

$$\left\langle \phi_I^{(m)} \left| \frac{d\phi_J^{(n)}}{dt} \right. \right\rangle = \dot{\mathbf{R}}_n \left\langle \phi_I^{(m)}(\overline{\mathbf{R}}_m) \left| \frac{d}{d\overline{\mathbf{R}}_n} \right| \phi_J^{(n)}(\overline{\mathbf{R}}_n) \right\rangle.$$

(A3.4)

Inserting the unity, as above, we can express the matrix elements (A3.4) as:

$$\left\langle \phi_I^{(m)} \left| \frac{d}{d\overline{\mathbf{R}}_n} \right| \phi_J^{(n)} \right\rangle = \sum_K \left\langle \phi_I^{(m)} | \phi_K^{(n)} \right\rangle \left\langle \phi_K^{(n)} \left| \frac{d}{d\overline{\mathbf{R}}_n} \right| \phi_J^{(n)} \right\rangle$$
$$= \sum_K \left\langle \phi_I^{(m)} \middle| \phi_K^{(n)} \right\rangle \mathbf{d}_{KJ}(\overline{\mathbf{R}}_n).$$

(A3.5)

Substituting Eq. (A2.3) for $\dot{a}_j^{(n)}$ into (A3.3), one can see that its off-diagonal terms are cancelled out by the terms of Eq. (A3.5). Thus, we obtain:

$$\left\langle \psi_m \left| \frac{d\psi_n}{dt} \right. \right\rangle = \left\langle \chi_m \left| \frac{d\chi_n}{dt} \right. \right\rangle \sum_{I,J} \left\langle \phi_I^{(m)} \middle| \phi_J^{(n)} \right\rangle \left(a_I^{(m)} \right)^* a_J^{(n)}$$
$$- \frac{i}{\hbar} \langle \chi_m | \chi_n \rangle \sum_{I,J} \left\langle \phi_I^{(m)} \middle| \phi_J^{(n)} \right\rangle \left(a_I^{(m)} \right)^* a_J^{(n)} V_J(\overline{\mathbf{R}}_n).$$

(A3.6)

Calculations of the electronic populations and other electronic properties in TDD representation requires the evaluation of the matrix elements $\left\langle \chi_m \middle| \left\langle \phi_I^{(m)} \middle| \phi_K(\mathbf{R}) \right\rangle \left\langle \phi_K(\mathbf{R}) \middle| \phi_J^{(n)} \right\rangle \middle| \chi_n \right\rangle$, for which an approximation can be used similar to the one for other matrix elements between trajectories

$$\left\langle \chi_m \middle| \left\langle \phi_I^{(m)} | \phi_K(\mathbf{R}) \right\rangle \left\langle \phi_K(\mathbf{R}) \middle| \phi_J^{(n)} \right\rangle \middle| \chi_n \right\rangle \approx \frac{1}{2} \left\{ \left\langle \chi_m \middle| \left\langle \phi_I^{(m)} \middle| \phi_K^{(m)} \right\rangle \left\langle \phi_K^{(m)} \middle| \phi_J^{(n)} \right\rangle \middle| \chi_n \right\rangle \right.$$
$$\left. + \left\langle \chi_m \middle| \left\langle \phi_I^{(m)} \middle| \phi_K^{(n)} \right\rangle \left\langle \phi_K^{(n)} \middle| \phi_J^{(n)} \right\rangle \middle| \chi_n \right\rangle \right\} = \frac{1}{2} \langle \chi_m | \chi_n \rangle \left\{ \left\langle \phi_K^{(m)} \middle| \phi_J^{(n)} \right\rangle \delta_{IK} + \left\langle \phi_I^{(m)} \middle| \phi_K^{(n)} \right\rangle \delta_{JK} \right\}$$

(A3.7)

References

[1] M. Ben-Nun, T.J. Martínez, Advances in Chemical Physics, John Wiley & Sons Inc, 2002, p 439.
[2] G.A. Worth, M.A. Robb, B. Lasorne, Mol. Phys. 106 (2008) 2077.
[3] G.W. Richings, I. Polyak, K.E. Spinlove, G.A. Worth, B. Burghardt, B. Lasorne, Int. Rev. Phys. Chem. 34 (2015) 269.
[4] G.A. Worth, I. Burghardt, Chem. Phys. Lett. 368 (2003) 502.
[5] A.L. Thompson, C. Punwong, T. Martinez, J. Chem. Phys. 370 (2010) 70.
[6] D.V. Makhov, W.J. Glover, T.J. Martinez, D.V. Shalashilin, J. Chem. Phys. 141 (2014) 054110.
[7] D.V. Makhov, K. Saita, T.J. Martinez, D.V. Shalashilin, Phys. Chem. Chem. Phys. 17 (2015) 3316.
[8] S.K. Reed, D.R. Glowacki, D.V. Shalashilin, Chem. Phys. 370 (2010) 223.
[9] K. Saita, M.G.D. Nix, D.V. Shalashilin, Phys. Chem. Chem. Phys. 15 (2013) 16227.
[10] K. Saita, D.V. Shalashilin, J. Chem. Phys. 137 (2012) 22A506.
[11] D.V. Shalashilin, J. Chem. Phys. 132 (2010) 244111.
[12] M. Ben-Nun, T.J. Martinez, J. Chem. Phys. 110 (1999) 4134.
[13] D.V. Shalashilin, M.S. Child, J. Chem. Phys. 128 (2008) 054102.
[14] D.V. Shalashilin, J. Chem. Phys. 130 (2009) 244101.
[15] P. Kramer, M. Saraceno, Geometry of the Time-Dependent Variational Principle in Quantum Mechanics, Springer, Berlin Heidelberg, 1981.
[16] I. Burghardt, H.-D. Meyer, L.S. Cederbaum, J. Chem. Phys. 111 (1999) 2927.
[17] T.J. Martínez, Chem. Phys. Lett. 272 (1997) 139.
[18] S. Fernandez-Alberti, A.E. Roitberg, T. Nelson, S. Tretiak, J. Chem. Phys. (2012) 137.
[19] S. Fernandez-Alberti, D.V. Makhov, S. Tretiak, D.V. Shalashilin, Phys. Chem. Chem. Phys. 18 (2016) 10028.
[20] M.V. Berry, Proc. R. Soc. London A. Math. Phys. Sci. 392 (1984) 45.
[21] C.A. Mead, D.G. Truhlar, J. Chem. Phys. 70 (1979) 2284.
[22] E.J. Heller, J. Chem. Phys. 75 (1981) 2923.
[23] M.F. Herman, Annu. Rev. Phys. Chem. 45 (1994) 83.
[24] M.F. Herman, E. Kluk, Chem. Phys. 91 (1984) 27.
[25] E. Kluk, M.F. Herman, H.L. Davis, J. Chem. Phys. 84 (1986) 326.
[26] W.H. Miller, J. Phys. Chem. A 105 (2001) 2942.
[27] E. Martin-Fierro, E. Pollak, J. Chem. Phys. (2007) 126.
[28] E. Wigner, Phys. Rev. 40 (1932) 749.
[29] K.Husimi, Proceedings of the Physico-Mathematical Society of Japan. 3rd Series, 1940, 22, 264.
[30] T.J. Martinez, M. BenNun, G. Ashkenazi, J. Chem. Phys. 104 (1996) 2847.
[31] T.J. Martinez, M. BenNun, R.D. Levine, J. Phys. Chem. 100 (1996) 7884.
[32] M. Ben-Nun, T.J. Martinez, Isr. J. Chem. 47 (2007) 75.
[33] S. Yang, J.D. Coe, B. Kaduk, T.J. Martinez, J. Chem. Phys. (2009) 130.
[34] M. Ben-Nun, T.J. Martínez, J. Phys. Chem. A 103 (1999) 6055.
[35] M. Ben-Nun, T.J. Martínez, J. Chem. Phys. 112 (2000) 6113.
[36] D.V. Makhov, T.J. Martinez, D.V. Shalashilin, Faraday Discuss. 194 (2016) 81.
[37] S.-Y. Ye, D. Shalashilin, A. Serafini, Phys. Rev. A (2012) 86.
[38] R.A.S.N. Marcus, Biochim. Biophys. Acta (BBA) - Rev. Bioenerg. 811 (1985) 265.
[39] N. Makri, J. Chem. Phys. A 102 (1998) 4414.

[40] E. Martin-Fierro, E. Pollak, J. Chem. Phys. 126 (2007) 164108.
[41] G. Stock, J. Chem. Phys. 103 (1995) 1561.
[42] H. Wang, M. Thoss, J. Chem. Phys. 119 (2003) 1289.
[43] H. Wang, M. Thoss, New J. Phys. 10 (2008) 115005.
[44] H. Wang, J. Chem. Phys. 113 (2000) 9948.
[45] H. Wang, M. Thoss, W.H. Miller, J. Chem. Phys. 112 (2000) 47.
[46] D.V. Shalashilin, Faraday Discuss. 153 (2011) 105.
[47] C. Symonds, D.V. Shalashilin, 2017, in preparation.
[48] B.G. Levine, J.D. Coe, A.M. Virshup, T. Martinez, J. Chem. Phys. 347 (2008) 3.
[49] R. Kopelman, M. Shortreed, Z.Y. Shi, W.H. Tan, Z.F. Xu, J.S. Moore, A. BarHaim, J. Klafter, Phys. Rev. Lett. 78 (1997) 1239.
[50] S. Mukamel, S. Tretiak, T. Wagersreiter, V. Chernyak, Science 277 (1997) 781.
[51] S. Tretiak, V. Chernyak, S. Mukamel, J. Chem. Phys. 105 (1996) 8914.
[52] S. Tretiak, W.M. Zhang, V. Chernyak, S. Mukamel, Proc. Natl. Acad. Sci. U.S.A. 96 (1999) 13003.
[53] M.J.S. Dewar, E.G. Zoebisch, E.F. Healy, J.J.P. Stewart, J. Am. Chem. Soc. 107 (1985) 3902.
[54] S. Fernandez-Alberti, V.D. Kleiman, S. Tretiak, A.E. Roitberg, J. Phys. Chem. A 113 (2009) 7535.
[55] S. Fernandez-Alberti, V.D. Kleiman, S. Tretiak, A.E. Roitberg, J. Phys. Chem. Lett. 1 (2010) 2699.
[56] S. Fernandez-Alberti, A.E. Roitberg, V.D. Kleiman, T. Nelson, S. Tretiak, J. Chem. Phys. (2012) 137.
[57] M. Ben-Nun, T. Martinez, J. Chem. Phys. Lett. 298 (1998) 57.
[58] E.F. Cromwell, A. Stolow, M.J.J. Vrakking, Y.T. Lee, J. Chem. Phys. 97 (1992) 4029.
[59] K. Kosma, S.A. Trushin, W. Fuss, W.E. Schmid, J. Phys. Chem. A 112 (2008) 7514.
[60] T. Mori, W.J. Glover, M.S. Schuurman, T.J. Martinez, J. Phys. Chem. A 116 (2012) 2808.
[61] R.J. Sension, B.S. Hudson, J. Chem. Phys. 90 (1989) 1377.
[62] V. Stert, H. Lippert, H.H. Ritze, W. Radloff, Chem. Phys. Lett. 388 (2004) 144.
[63] H. Tao, T.K. Allison, T.W. Wright, A.M. Stooke, C. Khurmi, J. van Tilborg, Y. Liu, R.W. Falcone, A. Belkacem, T.J. Martinez, J. Chem. Phys. (2011) 134.
[64] H. Tao, B.G. Levine, T.J. Martinez, J. Phys. Chem. A 113 (2009) 13656.
[65] A. Viel, R.P. Krawczyk, U. Manthe, W. Domcke, Angewandte Chemie-International Edition 42 (2003) 3434.
[66] A. Viel, R.P. Krawczyk, U. Manthe, W. Domcke, J. Chem. Phys. 120 (2004) 11000.
[67] P.V. Parandekar, J.C. Tully, J. Chem. Theory. Comput. 2 (2006) 229.
[68] P.V. Parandekar, J.C. Tully, J. Chem. Phys. 122 (2005) 094102.
[69] G.M. Roberts, C.A. Williams, H. Yu, A.S. Chatterley, J.D. Young, S. Ullrich, V.G. Stavros, Faraday Discuss. 163 (2013) 95.
[70] J. Wei, J. Riedel, A. Kuczmann, F. Renth, F. Temps, Faraday Discuss. 127 (2004) 267.
[71] C.T. Middleton, K. de La Harpe, C. Su, Y.K. Law, C.E. Crespo-Hernandez, B. Kohler, Annu. Rev. Phys. Chem. 60 (2009) 217.
[72] A.L. Sobolewski, W. Domcke, Chem. Phys. 259 (2000) 181.
[73] A.L. Sobolewski, W. Domcke, C. Dedonder-Lardeux, C. Jouvet, Phys. Chem. Chem. Phys. 1093 (2002) 4.
[74] Z. Lan, A. Dupays, V. Vallet, S. Mahapatra, W. Domcke, J. Photochem. Photobiol. Chem. 190 (2007) 177.
[75] V. Vallet, Z.G. Lan, S. Mahapatra, A.L. Sobolewski, W. Domcke, J. Chem. Phys. 123 (2005) 144307.
[76] M. Barbatti, J. Pittner, M. Pederzoli, U. Werner, R. Mitric, V. Bonacic-Koutecky, H. Lischka, Chem. Phys. 375 (2010) 26.
[77] V. Vallet, Z. Lan, S. Mahapatra, A.L. Sobolewski, W. Domcke, Faraday Discuss. 127 (2004) 283.
[78] Z. Lan, W. Domcke, V. Vallet, A.L. Sobolewski, S. Mahapatra, J. Chem. Phys. 122 (2005) 224315.
[79] S. Mahapatra, Acc. Chem. Res. 1004 (2009) 42.
[80] M.N.R. Ashfold, B. Cronin, A.L. Devine, R.N. Dixon, M.G.D. Nix, Science 312 (2006) 1637.
[81] M.N.R. Ashfold, A.L. Devine, R.N. Dixon, G.A. King, M.G.D. Nix, T.A.A. Oliver, Proc. Nat. Acad. Sci. U.S.A. 105 (2008) 12701.
[82] G.A. King, A.L. Devine, M.G.D. Nix, D.E. Kelly, M.N.R. Ashfold, Phys. Chem. Chem. Phys. 10 (2008) 6417.
[83] A.L. Devine, B. Cronin, M.G.D. Nix, M.N.R. Ashfold, J. Chem. Phys. 125 (2006) 184302.
[84] G.A. King, T.A.A. Oliver, M.G.D. Nix, M.N.R. Ashfold, J. Chem. Phys. 132 (2010) 064305.
[85] M.G.D. Nix, A.L. Devine, B. Cronin, M.N.R. Ashfold, J. Chem. Phys. (2007) 126.
[86] M.G.D. Nix, A.L. Devine, B. Cronin, R.N. Dixon, M.N.R. Ashfold, J. Chem. Phys. (2006) 125.
[87] A.G. Sage, M.G.D. Nix, M.N.R. Ashfold, Chem. Phys. 347 (2008) 300.
[88] A.J. van den Brom, M. Kapelios, T.N. Kitsopoulos, N.H. Nahler, B. Cronin, M.N.R. Ashfold, Phys. Chem. Chem. Phys. 7 (2005) 892.
[89] J.L. Palma, E. Atas, L. Hardison, T.B. Marder, J.C. Collings, A. Beeby, J.S. Melinger, J.L. Krause, V.D. Kleiman, A.E. Roitberg, J. Phys. Chem. C 114 (2010) 20702.
[90] C. Devadoss, P. Bharathi, J.S. Moore, J. Am. Chem. Soc. 118 (1996) 9635.
[91] M.R. Shortreed, S.F. Swallen, Z.Y. Shi, W.H. Tan, Z.F. Xu, C. Devadoss, J.S. Moore, R. Kopelman, J. Phys. Chem. B 101 (1997) 6318.
[92] S.F. Swallen, R. Kopelman, J.S. Moore, C. Devadoss, J. Mol. Struct. 485 (1999) 585.
[93] Z.F. Xu, M. Kahr, K.L. Walker, C.L. Wilkins, J.S. Moore, J. Am. Chem. Soc. 116 (1994) 4537.
[94] T. Nelson, S. Fernandez-Alberti, V. Chernyak, A.E. Roitberg, S. Tretiak, J. Phys. Chem. B 115 (2011) 5402.
[95] T. Nelson, S. Fernandez-Alberti, A.E. Roitberg, S. Tretiak, Acc. Chem. Res. 47 (2014) 1155.
[96] S. Hammes-Schiffer, J.C. Tully, J. Chem. Phys. 101 (1994) 4657.
[97] J.C. Tully, J. Chem. Phys. 1061 (1990) 93.
[98] J.C. Tully, Int. J. Quantum Chem. 40 (1991) 299.
[99] T. Nelson, S. Fernandez-Alberti, A.E. Roitberg, S. Tretiak, J. Chem. Phys. (2013) 138.
[100] M.N.R. Ashfold, G.A. King, D. Murdock, M.G.D. Nix, T.A.A. Oliver, A.G. Sage, Phys. Chem. Chem. Phys. 12 (2010) 1218.
[101] B. Cronin, A.L. Devine, M.G.D. Nix, M.N.R. Ashfold, Phys. Chem. Chem. Phys. 8 (2006) 3440.
[102] A.L. Devine, M.G.D. Nix, R.N. Dixon, M.N.R. Ashfold, J. Phys. Chem. A 112 (2008) 9563.
[103] M.G.D. Nix, A.L. Devine, B. Cronin, M.N.R. Ashfold, Phys. Chem. Chem. Phys. 8 (2006) 2610.
[104] A.L. Sobolewski, W. Domcke, ChemPhysChem 7 (2006) 561.
[105] B. Cronin, M.G.D. Nix, R.H. Qadiri, M.N.R. Ashfold, Phys. Chem. Chem. Phys. 6 (2004) 5031.
[106] R.N. Dixon, T.A.A. Oliver, M.N.R. Ashfold, J. Chem. Phys. (2011) 134.
[107] D.J. Hadden, G.M. Roberts, T.N.V. Karsili, M.N.R. Ashfold, V.G. Stavros, Phys. Chem. Chem. Phys. 14 (2012) 13415.
[108] T.N.V. Karsili, A.M. Wenge, S.J. Harris, D. Murdock, J.N. Harvey, R.N. Dixon, M.N.R. Ashfold, Chem. Sci. 4 (2013) 2434.
[109] M.G.D. Nix, A.L. Devine, R.N. Dixon, M.N.R. Ashfold, Chem. Phys. Lett. 463 (2008) 305.
[110] M. Staniforth, J.D. Young, D.R. Cole, T.N.V. Karsili, M.N.R. Ashfold, V.G. Stavros, J. Phys. Chem. A 118 (2014) 10909.
[111] D.J. Hadden, K.L. Wells, G.M. Roberts, L.T. Bergendahl, M.J. Paterson, V.G. Stavros, Phys. Chem. Chem. Phys. 13 (2011) 10342.
[112] A. Iqbal, M.S.Y. Cheung, M.G.D. Nix, V.G. Stavros, J. Phys. Chem. A 113 (2009) 8157.
[113] A. Iqbal, V.G. Stavros, J. Phys. Chem. A 114 (2009) 68.
[114] G.M. Roberts, A.S. Chatterley, J.D. Young, V.G. Stavros, J. Phys. Chem. Lett. 3 (2012) 348.
[115] G.M. Roberts, V.G. Stavros, Chem. Sci. 5 (2014) 1698.
[116] C.A. Williams, G.M. Roberts, H. Yu, N.L. Evans, S. Ullrich, V.G. Stavros, J. Phys. Chem. A 116 (2011) 2600.
[117] J.D. Young, M. Staniforth, A.S. Chatterley, M.J. Paterson, G.M. Roberts, V.G. Stavros, Phys. Chem. Chem. Phys. 16 (2014) 550.
[118] H. Yu, N.L. Evans, V.G. Stavros, S. Ullrich, Phys. Chem. Chem. Phys. 14 (2012) 6266.
[119] D.R. Glowacki, A.J. Orr-Ewing, J.N. Harvey, J. Chem. Phys. 134 (2011) 11.
[120] D.R. Glowacki, R.A. Rose, S.J. Greaves, A.J. Orr-Ewing, J.N. Harvey, Nat. Chem. 3 (2011) 850.
[121] S.J. Greaves, R.A. Rose, T.A.A. Oliver, D.R. Glowacki, M.N.R. Ashfold, J.N. Harvey, I.P. Clark, G.M. Greetham, A.W. Parker, M. Towrie, A.J. Orr-Ewing, Science 331 (2011) 1423.
[122] W. Barford, Electronic and Optical Properties of Conjugated Polymers, Oxford University Press, 2013.
[123] D.V. Makhov, W. Barford, Phys. Rev. B 81 (2010) 6.
[124] W. Barford, D.G. Lidzey, D.V. Makhov, A.J.H. Meijer, J. Chem. Phys. 133 (2010) 6.
[125] W. Barford, I. Boczarow, T. Wharram, J. Phys. Chem. A 115 (2011) 9111.
[126] M. Marcus, J. Coonjobeeharry, W. Barford, J. Chem. Phys. 144 (2016) 14.
[127] A. Kirrander, K. Saita, D.V. Shalashilin, J. Chem. Theory Comput. 12 (2016) 957.
[128] M.P. Minitti, J.M. Budarz, A. Kirrander, J. Robinson, T.J. Lane, D. Ratner, K. Saita, T. Northey, B. Stankus, V. Cofer-Shabica, J. Hastings, P.M. Weber, Faraday Discuss. 171 (2014) 81.
[129] H. Hellmann, Einführung in Die Quantenchemie F, Deuticke, Leipzig und Wien, 1937.
[130] R.P. Feynman, Phys. Rev. 56 (1939) 340.

Dmitry V. Makhov received his M.S. in Applied Mathematics and Physics from Moscow Institute of Physics and Technology and his Ph.D. in Chemical Physics from the Institute of Chemical Physics of Russian Academy of Sciences. Then he worked as a postdoc at the University of Montreal, University of California Davis and the University of Oxford. Currently he is a research fellow at the University of Leeds, and his scientific interests are focused on the development and applications of the method of direct ab initio quantum dynamics.

Sebastian Fernandez-Alberti is currently a Full Professor at National University of Quilmes (UNQ, Argentina) and Independent Researcher at the National Council for Scientific and Technical Research (CONICET, Argentina). He received his degree in 1993 from the National University of La Plata (UNLP, Argentina) and his Ph.D. in Molecular Physics in 1999 from the University of Paul Sabatier (Toulouse, France). His research interests include excited-state nonadiabatic dynamics simulations in extended conjugated molecules, electronic and vibrational relaxation, and intramolecular energy redistribution in polyatomic molecules, and protein dynamics analysis using collective coordinates.

Christopher Symonds earned his MPhys in Physics in 2012 and his Ph.D. in Computational Chemistry in 2016, both from the University of Leeds. He is currently a Postdoctoral Associate in the research group of Prof. Dmitrii Shalashilin at the University of Leeds. His research interests include the development and application of computational quantum moleculardynamics techniques.

Dmitrii V Shalashilin received his PhD in Physics and Mathematics in 1987 from Moscow Institute of Physics and Technology under the supervision of Prof. M. Ya Ovchinnikova and Prof E.E. Nikitin. He was employed as a research scientist at the theoretical department of the Institute of Chemical Physics USSR and Russian Academy of Sciences until 1993. After that he took several temporary positions at Institute of Chemistry National University of Mexico, Oklahoma State University, University of Massachusetts, and at Oxford University in the group of Prof. M.S. Child, where he started the development of new trajectory and Coherent State based methods of quantum dynamics. In 2006 he was employed as a lecturer at the University of Leeds, where now he is a Professor of Computational Chemistry. His current research interests are focused on the new methods of quantum dynamics and classical molecular dynamics of biomolecules.